



Contents lists available at ScienceDirect

Remote Sensing of Environment

journal homepage: www.elsevier.com/locate/rse

Direct estimation of photosynthetic CO₂ assimilation from solar-induced chlorophyll fluorescence (SIF)

Zhunqiao Liu^a, Feng Zhao^b, Xinjie Liu^c, Qiang Yu^{a,d}, Yunfei Wang^{a,e,f}, Xiongbiao Peng^{e,f}, Huanjie Cai^{e,f}, Xiaoliang Lu^{a,*}

^a State Key Laboratory of Soil Erosion and Dryland Farming on the Loess Plateau, Northwest A&F University, Yangling, Shaanxi 712100, China

^b School of Instrumentation Science and Opto-Electronics Engineering, Beihang University, Beijing 100083, China

^c Key Laboratory of Digital Earth Science, Aerospace Information Research Institute, Chinese Academy of Sciences, Beijing 100094, China

^d Key Laboratory of Water Cycle and Related Land Surface Processes, Institute of Geographic Sciences and Natural Resources Research, Chinese Academy of Sciences, Beijing 100101, China

^e Key Laboratory of Agricultural Soil and Water Engineering in Arid Area of Ministry of Education, Northwest A&F University, Yangling, China

^f Institute of Water Saving Agriculture in Arid Regions of China (IWSA), Northwest A&F University, Yangling, China

ARTICLE INFO

Editor: Jing M. Chen

Keywords:

Solar-induced chlorophyll fluorescence
Gross primary productivity (GPP)
Mechanistic light response model
Nonphotochemical quenching (NPQ)
Quantum yield of photosystem II (Φ_p)
Direct estimation

ABSTRACT

Much progress has been made in predicting terrestrial gross primary productivity (GPP) from solar-induced chlorophyll fluorescence (SIF). However, SIF-GPP relationships are mostly built by statistically relating top-of-canopy (TOC) SIF observations (SIF_{TOC}) to eddy covariance flux-tower GPP estimates. We developed a process-based model, based on the mechanistic light response (MLR) model, to mechanistically link SIF_{TOC} with the photosynthetic activity of vegetation. To apply this mechanistic model at the canopy scale, we 1) reformulate the equations by replacing the fraction of open PSII reaction centers (q_l) and the maximum quantum yield of photosystem II (Φ_{pmax}) with nonphotochemical quenching (NPQ) and the quantum yield of photosystem II (Φ_p); 2) reconstruct hemispherical broadband SIF fluxes at photosystem II (PSII) from the directional observed SIF_{TOC} that is contributed from photosystem I and II; 3) estimate other key parameters including K_{DF} (ratio between the rate constants for constitutive heat loss and fluorescence), C_c (chloroplastic CO₂ partial pressure), and Γ^* (chloroplastic compensation point of CO₂) at the canopy scale based on assumptions and in-situ measurements. A comparison against flux-tower based GPP at a winter-wheat study site, demonstrates that the modeled GPP, driven by SIF_{TOC} at 760 nm, air temperature, incoming photosynthetically active radiation (PAR), and directional reflectance in the red and near-infrared region, is able to quantify canopy photosynthesis with good accuracy at both half-hourly ($R^2 = 0.85$, RMSE = 5.62 $\mu\text{mol m}^{-2} \text{s}^{-1}$, rRMSE = 9.10%) and daily ($R^2 > 0.90$, RMSE = 3.25 $\mu\text{mol m}^{-2} \text{s}^{-1}$ and rRMSE = 8.69%) scales. The present model enhances our ability to mechanistically estimate GPP with SIF at the canopy scale, an essential step to model carbon uptake using satellite SIF at regional and global scales.

1. Introduction

During photosynthesis, absorbed photon energy may be used in three alternative pathways: photochemistry, heat loss (nonphotochemical quenching, NPQ), or re-emitted as chlorophyll *a* fluorescence (ChlF) in the spectral range 640–850 nm (Meroni et al., 2009; Mohammed et al., 2019; Porcar-Castell et al., 2021). Leaf-level pulse-amplitude modulation (PAM) or “active” measurements of ChlF, often combined with leaf-level measurements of gas exchange, have been used for more than three decades to quantify the probability of an absorbed photon taking a given

pathway and relate that probability to plant photosynthetic status (Magney et al., 2017; Meeker et al., 2021; Zhang et al., 2019). In the last ten years, improvements in remote sensing instrumentation and retrieval algorithms have enabled the passive detection of solar-induced chlorophyll fluorescence (SIF) within both Fraunhofer lines and atmospheric oxygen absorption bands (i.e., O₂-B and O₂-A and at 687 nm and 760 nm, respectively) from ground-based, airborne, and spaceborne remote-sensing platforms (Du et al., 2020; Frankenberg et al., 2014; Yang et al., 2015). SIF has an advantage over actively induced ChlF (i.e., PAM fluorescence) in that it can be used to track plant

* Corresponding author.

E-mail address: luxiaoliang@nwfau.edu.cn (X. Lu).

<https://doi.org/10.1016/j.rse.2022.112893>

Received 14 October 2021; Received in revised form 28 December 2021; Accepted 4 January 2022

Available online 17 January 2022

0034-4257/© 2022 Elsevier Inc. All rights reserved.

photosynthesis at scales larger than single leaves under natural conditions.

A number of studies have shown that SIF observations have a strong correlation with gross primary production (GPP) in a variety of terrestrial ecosystems, including crops (He et al., 2020), deciduous forests (Yang et al., 2015), and evergreen forests (Kimm et al., 2021; Magney et al., 2019a). Currently, statistical regressions are typically used to estimate GPP from SIF. Specifically, a model (e.g., a regression) describing the SIF-GPP relationship for a given plant functional type (PFT) is first trained by comparing SIF observations and flux-tower based GPP; this optimized model is then used, with satellite measurements of SIF as inputs, to generate GPP estimates at regional and global scales. Although such methods are simple and efficient, one should be aware of their limitations: (1) spatial heterogeneity may cause large uncertainties (Desai et al., 2008), especially in sparsely instrumented regions, (2) the established SIF-GPP relationships may not always hold in space or time due to parameter variability within a PFT (Xiao et al., 2011), and (3) it is difficult to mechanistically attribute variations in SIF-GPP relationships to relevant structural and/or physiological factors.

Recently, Gu et al. (2019a) developed the mechanistic light response (MLR) model which explicitly considers the key mechanisms linking ChF emission with C3 and C4 photosynthesis. They showed that photosynthetic CO₂ assimilation is a function of the broadband (640–850 nm) chlorophyll fluorescence flux density emitted from photosystem II (PSII), the fraction of open PSII reaction centers (q_L , Kramer et al., 2004), the maximum quantum yield of photosystem II ($\Phi_{P_{max}}$), the ratio between the rate constant for constitutive heat loss (K_D) and fluorescence emission (K_F) in PSII (K_{DF}), and the probability that fluorescence photons escape from photosystem II reaction centers to the canopy (f_{esc_P-C}). The MLR model provides a mechanistic framework potentially allowing estimation of GPP from top-of-canopy (TOC) SIF observations, but a few challenging issues have to be addressed before it can be used for practical applications: (1) extracting the PSII contribution to TOC SIF (f_{PSII}), (2) estimating the key parameters, especially q_L and K_{DF} , (3) linking measurements of narrowband SIF with broadband SIF, and (4) eliminating the impacts of canopy structure and varying solar-view geometries on TOC SIF.

In this study, we establish a framework to directly quantify canopy CO₂ assimilation from TOC SIF observations. We show that the roles of q_L and $\Phi_{P_{max}}$ in the original MLR model can be replaced by the quantum yield of photosystem II (Φ_P) and NPQ. We also provide the methods for estimating Φ_P , NPQ, f_{PSII} , and f_{esc_P-C} at the canopy scale. A leaf-level measurement system, developed to determine K_{DF} , is described, and the performance of the proposed model for estimating photosynthetic CO₂ assimilation is evaluated using flux-tower based GPP estimates from a winter-wheat study site.

2. Flux-tower site and data

2.1. Study site

The automatic spectral, gas-flux, and meteorological observations were made at the Yangling experimental-agriculture site (108° 04' E, 34° 17' N) in northwest China during the wheat-growing season of 2021. The Yangling site is located in the Institute of Water-saving Agriculture in Arid Areas of China (IWSA), Northwest A&F University, Shannxi Province, China (Fig. 1a). Yangling has a semi-arid to sub-humid climate with an average annual precipitation of 630 mm and an average annual air temperature of 12.9 °C (Yu et al., 2016). The topography is flat, and the soil is silty clay loam with the bulk density of 1.35 g cm⁻³, the field capacity of 0.42 m³ m⁻³, the permanent wilting point of 0.0875 m³ m⁻³ (Wang et al., 2020). Flood irrigation was applied when the soil water content was less than 60% of the field capacity (Yu et al., 2016). The crop type during the study period was winter wheat (*Triticum aestivum*, cv. Xinong 979), sown on 20 October 2020 and harvested on 10 June 2021. The winter wheat was planted in rows and reached a maximum crop height of 90 cm. Data collection started on 16 December 2020 and ended shortly before harvest on 8 June 2021, a period encompassing the full range of growing stages: tillering (Fig. 1b), erecting (Fig. 1c), jointing, booting, flowering, and maturity (Fig. 1 e-f).

2.2. Tower-based SIF data

An automatic, six-channel SIF instrument (AUTOSIF-2-8, Bergsun

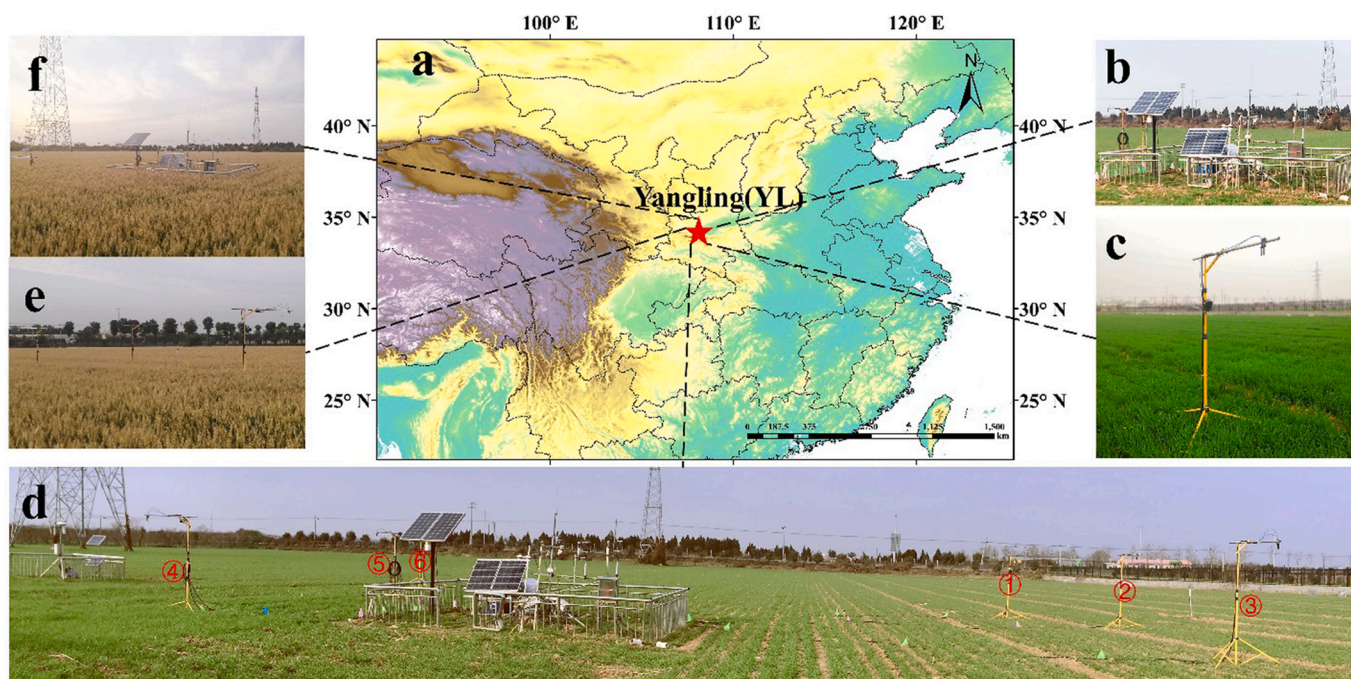


Fig. 1. The Yangling study site. (a) A regional map showing the location of the site in northwest China. (b–f) Photographs of the SIF measurement system, showing the six vegetation targets (labeled in d), and the flux measurement system.

Inc., Beijing, China) was deployed on six tripods about 2 m above the plant canopy to sample outgoing canopy radiance around the flux tower (Fig. 1d). This six-channel system reduces the footprint mismatch between SIF and fluxes measurements compared with SIF-measuring systems which have only a single vegetated target. The system contains a customized spectroradiometer (QE Pro, Ocean Optics, Dunedin, Florida, USA) with a signal-to-noise ratio of 1000, a spectral resolution of 0.34 nm, a sampling interval of 0.17 nm, and a spectral range of 645–805 nm. An optical multiplexer (MPM-2000, Ocean Optics, Dunedin, Florida, USA) was used to switch between a channel collecting the downwelling solar irradiance using a cosine corrector (CC-3, Ocean Optics, Dunedin, Florida, USA), a blind channel for correcting dark current, and six nadir-looking bare fibers with a field of view of 25° to obtain upwelling radiance. Hence, the SIF instrument had six measurement footprint circles each with a diameter of about 0.9 m. Both the spectroradiometer and multiplexer were enclosed in a dry, temperature-controlled container at 25 ± 1 °C. After correcting dark current and optimizing integration time, the “sandwich” method (downwelling-upwelling-downwelling) proposed by Meroni et al. (2008) was applied to reduce the negative impacts of unstable weather conditions (e.g., moving clouds). We performed a radiometric and spectral calibration of the system before installation.

We used the singular vector decomposition (SVD) method (Chang et al., 2020; Guanter et al., 2013; Liu et al., 2021) to retrieve SIF from the continuous spectral measurements. The SVD approach assumes that the SIF-free spectrum can be expressed as a linear combination of singular vectors obtained from a SIF-free training dataset (Guanter et al., 2012; Guanter et al., 2013), which, in this study, consisted of the continuous downwelling solar spectral measurements. The SVD approach does not require strictly synchronous measurements of downwelling irradiance and upwelling radiance, meaning that the negative impact of irradiance and radiance measurement mismatch on SIF retrieval can be kept to a minimum (Chang et al., 2020; Gu et al., 2019b). A spectral fitting window of 740–780 nm was adopted to retrieve TOC SIF observations in the near-infrared band (Liu et al., 2021). The retrieved SIF values were then aggregated into 30-min average data.

2.3. Eddy-covariance flux and meteorological measurements

An eddy-covariance (EC) system, measuring the CO₂ flux, was mounted on an adjustable-height tripod near the spectral measurement system at the Yangling site during the wheat growing season (Fig. 1 b–d). The site was large enough to accommodate the ~120 m fetch of the EC system. The EC system contained an open-path infrared gas analyzer (LI-7500A; LICOR, Lincoln, NE, USA) and a three-dimensional sonic anemometer (CSAT-3, Campbell Scientific, Logan, UT, USA). The sensors were installed at 2 m above the ground and pointed towards the prevalent wind direction. Relative humidity (RH) and air temperature (T_{air}) (HMP60, Vaisala Inc., Helsinki, Finland), global incoming short-wave radiation (R_g) (LI-200SZ, LI-COR, Lincoln, NE, USA), and photosynthetically active radiation (PAR) (LI-190SA, LI-COR, Lincoln, NE, USA) were measured 1.5 m above the soil surface during the growing season. Soil temperature (T_{soil}) and soil volumetric water content (SWC, $\text{m}^3 \text{m}^{-3}$) were observed at three depths (20, 40, and 60 cm below the ground surface) using a dielectric permittivity meter (Model 5TM, METEX Environment, Pullman, WA, USA). Thirty-minute averaged values of all the meteorological variables mentioned above were recorded by a datalogger (CR1000, Campbell Scientific, Logan, UT, USA).

The EddyPro 7 (LI-COR Inc., Lincoln, Nebraska, USA) software was used to convert the raw data (10 Hz) into 30-min fluxes of net ecosystem exchange (NEE). Poor quality flux data (flag 2) were rejected. Unreasonable flux data, such as CO₂ fluxes outside of the range -50 to $50 \mu\text{mol m}^{-2} \text{s}^{-1}$, sensible heat fluxes less than -200 W m^{-2} or greater than 500 W m^{-2} , and latent heat fluxes less than -200 W m^{-2} or greater than 800 W m^{-2} were also rejected (Wagle and Kakani, 2014). Furthermore,

flux data recorded during periods of precipitation, sensor malfunction, or during calm conditions (when the friction velocity was less than 0.1 m s^{-1}) were also excluded (Liu et al., 2020; Wagle et al., 2019). The REdDyProc-based online tool developed by the Max Planck Institute for Biogeochemistry was used to fill gaps in the data and to partition the CO₂ flux into its ecosystem respiration and GPP components using NEE, RH, T_{air} , T_{soil} , and R_g as inputs (<https://www.bgc-jena.mpg.de/REddyProc/brew/REddyProc.rhtml>). The gap-filling algorithm in REdDyProc can fill missing values in both the meteorological variables (T_{air} , R_g , and VPD) and the flux data (Falge et al., 2001; Reichstein et al., 2005; Wutzler et al., 2018). The daytime-based partitioning approach (Lasslop et al., 2010) was used to estimate ecosystem respiration (ER) by fitting a light-response curve between NEE and R_g (Falge et al., 2001; Lloyd and Taylor, 1994). Then, 30-min GPP values were obtained as the difference between NEE and ER.

3. Framework to estimate GPP using SIF observations

3.1. Reformulation of the MLR model

The MLR model (Gu et al., 2019a) shows that the actual rate of linear electron transport (J , $\mu\text{mol m}^{-2} \text{s}^{-1}$) can be estimated from SIF, q_L , and other parameters. However, q_L has been studied relatively little (Gu et al., 2019a), which may limit its practical usage (see the Discussion section). To the best of our knowledge, there is no well-evaluated model of q_L at the canopy scale. To obtain J and GPP from SIF, we can replace q_L with other photosynthetic parameters that can be measured or modeled as a function of environmental conditions. The fundamental relationship between SIF and J is (Gu et al., 2019a):

$$J = \frac{K_P \times \text{SIF}_{\text{TOC_FULL_PSII}}}{K_F \times f_{\text{esc_P-C}}} \quad (1)$$

where K_P is the rate constant of photochemical quenching, K_F is the rate constant for fluorescence emission in PSII that is a presumptive constant scalar (Zaks et al., 2012), $\text{SIF}_{\text{TOC_FULL_PSII}}$ is TOC broadband SIF (640–850 nm) emitted from PSII ($\mu\text{mol m}^{-2} \text{s}^{-1}$), and $f_{\text{esc_P-C}}$ is the probability that a SIF photon escapes from the PSII light reactions inside the leaves to the top of the canopy (Appendix A). It is noteworthy that $\text{SIF}_{\text{TOC_FULL_PSII}}/f_{\text{esc_P-C}}$ represents the broadband total (all leaves in the canopy) SIF flux density ($\mu\text{mol m}^{-2} \text{s}^{-1}$) emitted by PSII which is hereafter referred to as $\text{SIF}_{\text{TOT_FULL_PSII}}$. We also have (van der Tol et al., 2014):

$$K_P = \left(\frac{F_m' - F_s}{F_s} \right) \times (K_N + K_F + K_D) \quad (2a)$$

$$K_N = \left(\frac{F_m - F_m'}{F_m'} \right) \times (K_F + K_D) \quad (2b)$$

where K_N is the rate constant for regulated energy-dependent heat dissipation; F_s is the steady-state fluorescence yield; F_m and F_m' are the maximum fluorescence chlorophyll yields from dark-adapted and light-adapted states, respectively. Note that NPQ and Φ_P can be expressed as (Bilger and Björkman, 1990; Genty et al., 1989):

$$\text{NPQ} = \frac{F_m - F_m'}{F_m'} \quad (3a)$$

$$\Phi_P = \frac{F_m' - F_s}{F_m'} \quad (3b)$$

By inserting Eq. (3a) into Eq. (2b), we obtain $\text{NPQ} = K_N/(K_F + K_D)$. Meanwhile, Eq. (3b) can be rewritten as:

$$\frac{\Phi_P}{1 - \Phi_P} = \frac{F_m' - F_s}{F_s} \quad (4)$$

Combining Eqs. (2a), (2b), (3a), and (4), we have:

$$K_P = \frac{\Phi_P}{1 - \Phi_P} \times (1 + \text{NPQ}) \times (K_F + K_D) \quad (5)$$

Note that $K_{DF} = K_D/K_F$, so Eq. (5) can be expressed as:

$$\frac{K_P}{K_F} = \frac{\Phi_P \times (1 + NPQ) \times (1 + K_{DF})}{(1 - \Phi_P)} \quad (6)$$

By replacing the ratio of K_P to K_F in Eq. (1) with Eq. (6), we have:

$$J = \frac{\Phi_P \times (1 + NPQ) \times (1 + K_{DF}) \times SIF_{TOC_FULL_PSII}}{(1 - \Phi_P) \times f_{esc_P-C}} \quad (7)$$

Under the assumptions that Rubisco (ribulose 1,5-bisphosphate carboxylase/oxygenase) and TPU (triose phosphate utilization) limitations are ignored, and insufficient NADPH (Nicotinamide adenine dinucleotide phosphate) limits the regeneration of the RuBP (ribulose-1,5-bisphosphate) (Gu and Sun, 2014), GPP for C3 and C4 species can be expressed by the mechanistic equation (Gu et al., 2019a):

$$GPP = \begin{cases} \frac{C_c - \Gamma^*}{4C_c + 8\Gamma^*} \times \frac{\Phi_P \times (1 + NPQ) \times (1 + K_{DF}) \times SIF_{TOC_FULL_PSII}}{(1 - \Phi_P) \times f_{esc_P-C}} & \text{C3} \\ \frac{1 - \zeta}{3} \times \frac{\Phi_P \times (1 + NPQ) \times (1 + K_{DF}) \times SIF_{TOC_FULL_PSII}}{(1 - \Phi_P) \times f_{esc_P-C}} & \text{C4} \end{cases} \quad (8)$$

where C_c is the chloroplastic CO_2 partial pressure (μbar or $\mu\text{mol mol}^{-1}$); Γ^* is the chloroplastic compensation point of CO_2 (μbar) (Gu et al., 2019a; Long and Bernacchi, 2003); ζ is the fraction of total electron transport of mesophyll and bundle sheath allocated to mesophyll, assumed to be 0.4 (von Caemmerer, 2000). Eq. (8) provides a basis for quantifying CO_2 assimilation via measurement of fluorescence radiance in practical applications. Below, we provide the methods to estimate these key parameters and variables at the canopy scale. The procedure for quantifying GPP from the observed SIF is shown in Fig. 2.

3.2. Estimation of $SIF_{TOT_FULL_PSII}$

3.2.1. Separating the contribution of PSII to TOC SIF

SIF emission measured at the canopy scale is narrowband (e.g., 760 nm) and contains contributions from both photosystem I (PSI) and photosystem II (PSII). As a first step in applying Eq. (8), the contribution of PSI to TOC SIF observations should be excluded. TOC SIF emission can be represented as a linear combination of PSI and PSII fluorescence radiance (Bacour et al., 2019; Magney et al., 2019b). In particular, the contribution of PSII to TOC SIF at 760 nm ($SIF_{TOC_760_PSII}$, $\text{mW m}^{-2} \text{nm}^{-1} \text{sr}^{-1}$) can be expressed as (Bacour et al., 2019):

$$SIF_{TOC_760_PSII} = f_{PSII} \times SIF_{TOC_760} \quad (9a)$$

$$f_{PSII} = \frac{m_2 \times \varepsilon}{m_1 + m_2 \times \varepsilon} \quad (9b)$$

where f_{PSII} (%) represents the contribution of PSII fluorescence to SIF_{TOC_760} ; ε is a factor controlling the contribution from PSII fluorescence. Based on a large number of SCOPE (Soil Canopy Observation of Photosynthesis and Energy fluxes) simulations, Bacour et al. (2019) showed that, at 760 nm, m_1 and m_2 were equal to 0.00561 and 0.00917, respectively. The parameters m_1 and m_2 (Eq. (9b)) are determined by isolated PSI and PSII fluorescence emission spectra at 760 nm measured in very diluted particle suspensions of light-harvesting complexes (Pedrós et al., 2010). They can be considered as the most suitable reference fluorescence emission spectra in simulation (Franck et al., 2002; Pedrós et al., 2008). The ratio between SIF photons emitted from PSI at a given wavelength and the counterpart from PSII is not altered in the SIF scattering and (re)absorption processes. Thus, at a specific wavelength (i.e., 760 nm in this study), the relative contribution of PSI and PSII SIF at canopy level should be equal to that of the photosystem

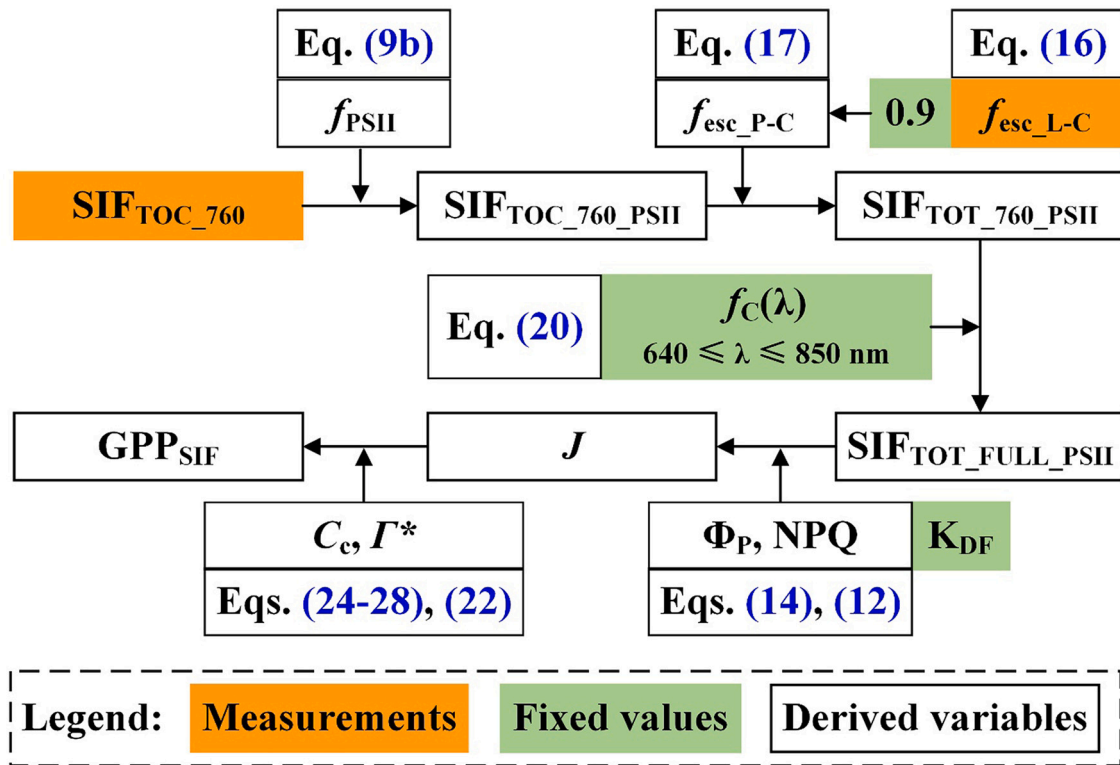


Fig. 2. Flowchart for quantifying canopy CO_2 assimilation from solar-induced fluorescence (SIF). SIF_{TOC_760} , top-of-canopy (TOC) SIF at 760 nm; f_{PSII} , photosystem II (PSII) contribution to SIF_{TOC_760} ; $SIF_{TOC_760_PSII}$, contribution of PSII to TOC SIF at 760 nm; f_{esc_P-C} , the probability that a SIF photon escapes from the PSII light reactions to the top of the canopy; f_{esc_L-C} , the probability of a fluorescence photon escaping from leaf level to canopy level; 0.9, the escape probability of SIF photon from the photosystems to the leaf surface; $SIF_{TOT_760_PSII}$, total SIF emitted from all leaves in the canopy at photosystem level at 760 nm; $f_c(\lambda)$, the conversion ratio of $SIF_{TOT_760_PSII}$ to $SIF_{TOT_FULL_PSII}$ at a given wavelength λ ($640 \leq \lambda \leq 850$ nm); $SIF_{TOT_FULL_PSII}$, broadband total (all leaves in the canopy) SIF flux density emitted by PSII; Φ_P , the quantum yield of photochemical quenching in PSII; NPQ, nonphotochemical quenching; J , linear electron transport; Γ^* , chloroplastic compensation point of CO_2 ; C_c , Chloroplastic CO_2 partial pressure; GPP_{SIF} , gross primary productivity deriving from SIF observations.

(PS) level. ε is estimated as the ratio of the fluorescence yield in PSII at the steady-state condition (Φ_F) to the minimum fluorescence yield with a maximum proportion of open PSII reaction centers (Φ_{F0}) (Bacour et al., 2019):

$$\varepsilon = \frac{\Phi_F}{\Phi_{F0}} \quad (10)$$

Here, Φ_{F0} is the reference fluorescence yield under dark-adapted conditions, and Φ_F can be estimated from Φ_p , K_D , K_N , and K_F (Bacour et al., 2019; Koffi et al., 2015; Lazár, 2015; Lee et al., 2015; Porcar-Castell et al., 2014; van der Tol et al., 2014):

$$\Phi_F = \frac{K_F}{K_D + K_F + K_N} \times (1 - \Phi_p) \quad (11)$$

Both K_D and K_F remain constant (Porcar-Castell, 2011). For simplicity, the four rate constants of the deexcitation pathways are expressed in units relative to $(K_D + K_F)$ and K_D and K_F are assumed to have values of 0.9 and 0.1, respectively (see the Estimating of K_{DF} section). Accordingly, NPQ should be equal to K_N due to $NPQ = K_N/(K_F + K_D)$. Because the maximum photochemical yield, Φ_{Pmax} , was assumed to be 0.8 (van der Tol et al., 2014), the maximum value of K_p was set to 4, resulting in $\Phi_{F0} = 0.02$ ($K_N = 0$). However, K_N , the first-order constant rate for a regulated process of thermal dissipation, varies with environmental conditions and can be modeled as a function of T_{air} and PAR (Bacour et al., 2019):

$$K_N = a \times \chi^c \times \frac{1 + b}{b + \chi^c} \times \frac{\exp(d \times T_{air} + e)}{PAR^f} \quad (12)$$

The fitting parameters, a (16.042), b (5.74), c (2.167), d (-0.014), e (-0.00437), and f (0.00576), are provided by Bacour et al. (2019). χ is defined as (van der Tol et al., 2014):

$$\chi = 1 - \frac{\Phi_p}{\Phi_{Pmax}} \quad (13)$$

where Φ_{Pmax} is assumed to be 0.8 and Φ_p is constrained by the most limiting factors between the carboxylation rate and electron transport rate (Bacour et al., 2019; Maxwell and Johnson, 2000; Porcar-Castell et al., 2014; van der Tol et al., 2014):

$$\Phi_p = \frac{\min(A_C, A_J)}{APAR \times \beta} \times \frac{4C_c + 8\Gamma^*}{C_c - \Gamma^*} \quad (14)$$

where A_C and A_J represent Rubisco-limited and RuBP-limited gross CO_2 assimilation ($\mu\text{mol m}^{-2} \text{s}^{-1}$), respectively (Yin and Struik, 2009). A_C is determined by the maximum carboxylation capacity of Rubisco at 25 °C (V_{cmax25} , $\mu\text{mol m}^{-2} \text{s}^{-1}$), C_c and Γ^* . A_J is determined by APAR (absorbed PAR, $\mu\text{mol m}^{-2} \text{s}^{-1}$) and the maximum capacity of the electron transport rate (J_{max} , $\mu\text{mol m}^{-2} \text{s}^{-1}$), C_c and Γ^* . In detail, J_{max} is calculated from T_{air} and J_{max} at 25 °C (J_{max25} , $\mu\text{mol m}^{-2} \text{s}^{-1}$) (June et al., 2004): the ratio J_{max25}/V_{cmax25} for C3 species is linearly related to T_{air} with a slope of 0.035 and intercept of 2.59 (Bacour et al., 2019; Kattge and Knorr, 2007). In this study, V_{cmax25} of winter wheat was set as 60 $\mu\text{mol m}^{-2} \text{s}^{-1}$ (Bacour et al., 2019). β is the proportion of absorbed PAR received by PSII, assumed to be 0.5 (Galmés et al., 2007; Hendrickson et al., 2004; Maxwell and Johnson, 2000). APAR is estimated from directional reflectance (see below). After determining C_c and Γ^* (Section 3.4), Eq. (14) is used to approximate Φ_p , which is then used to calculate J from Eq. (7). Note that Φ_p from Eq. (14) is a function of photosynthetic parameter (i.e., V_{cmax25}), leaf biochemical trait (i.e., chlorophyll content), canopy structure (i.e., f_{APAR}), and environmental factors (i.e., PAR and T_{air}). V_{cmax25} is species-specific and assigned a fixed value for the winter wheat. Thus, Φ_p estimated from Eq. (14) is considered to contain limited information on plant physiology. As a consequence, simply using the product $\Phi_p \times APAR$ may result in a bias in the estimate of J .

3.2.2. Downscaling from TOC to photosystem level

Next, the directional $SIF_{TOC,760,PSII}$ ($\text{mW m}^{-2} \text{nm}^{-1} \text{sr}^{-1}$) must be

downscaled from the canopy level to the photosystem level, namely $SIF_{TOT,760,PSII}$ ($\text{mW m}^{-2} \text{nm}^{-1}$), by dividing by the canopy SIF escape probability at 760 nm ($f_{esc,p-c}$ is for 760 nm, hereafter in this paper) and integrating over the hemispherical space:

$$SIF_{TOT,760,PSII} = \pi \times \frac{SIF_{TOC,760,PSII}}{f_{esc,p-c}} \quad (15)$$

Zeng et al. (2019) showed that the probability of a fluorescence photon escaping from leaf level to canopy level ($f_{esc,L-C}$) could be expressed as:

$$f_{esc,L-C} = \frac{NIR_V}{f_{APAR}} \quad (16)$$

where NIR_V is the product of the normalized difference vegetation index (NDVI) and canopy reflectance in the NIR region (Badgley et al., 2017), and f_{APAR} is the photosynthetically active radiation absorption efficiency. To calculate NIR_V and NDVI, we used 680 nm for red reflectance (R_{680}) and 755 nm for NIR reflectance (R_{755}). The escape probability of SIF photon from the photosystems to the leaf surface can be approximated by the leaf albedo that is rather stable with a value around 0.9 in the NIR region (Liu et al., 2020; Lu et al., 2020). Consequently, $f_{esc,p-c}$ in the NIR bands can be estimated as:

$$f_{esc,p-c} = 0.9 \times f_{esc,L-C} \quad (17)$$

Liu et al. (2019) showed that f_{APAR} could be estimated from the wide dynamic range vegetation index (WDRVI, Gitelson (2004)):

$$f_{APAR} = \psi \times f_{APARgreen} \quad (18a)$$

$$f_{APARgreen} = 0.516 \times WDRVI + 0.726 \quad (18b)$$

where $f_{APARgreen}$ is the fraction of PAR absorbed by the green leaves of a canopy; ψ is a coefficient factor assumed to be 0.79 in this study because leaf chlorophyll content values, measured by a chlorophyll concentration meter (MC-100, Apogee Instruments, Inc., Logan, UT, USA), were higher than 20 $\mu\text{g cm}^{-2}$ (Du et al., 2017; Siegmund et al., 2021). The WDRVI is defined as:

$$WDRVI = \frac{0.1 \times R_{755} - R_{680}}{0.1 \times R_{755} + R_{680}} \quad (19)$$

3.2.3. Reconstructing broadband SIF at photosystem level

We then need to reconstruct broadband $SIF_{TOT,FULL,PSII}$ from narrowband $SIF_{TOT,760,PSII}$: PSII SIF emitted from all leaves in the canopy at a given wavelength λ ($SIF_{TOT,\lambda,PSII}$, $\text{mW m}^{-2} \text{nm}^{-1}$) over the spectral range of 640–850 nm can be estimated from $SIF_{TOT,760,PSII}$. Based on a PSII SIF spectrum dataset simulated by the Soil Canopy Observation of Photosynthesis and Energy (SCOPE) model (version 1.73; van der Tol et al. (2009)), we used the SVD technique (Zhao et al., 2014) to investigate the relationship between $SIF_{TOT,\lambda,PSII}$ and $SIF_{TOT,760,PSII}$. To make this dataset represent the majority of actual scenes, a total of 6720 samples with different leaf biochemical and leaf structural properties, canopy structure, and sun-canopy-sensor geometry were generated to simulate SIF at PS level (Text S1). The remaining input parameters were fixed at their default values. The SVD analysis showed that the first principal component (PC1) explained more than 99% of the variance in this simulated dataset, suggesting that the spectral shape of PSII SIF remains roughly stable throughout the leaf and canopy structural effects, allowing the conversion ratio ($f_C(\lambda)$, see Text S1 for details) of $SIF_{TOT,\lambda,PSII}$ to $SIF_{TOT,760,PSII}$ to be estimated by PC1. $f_C(\lambda)$ is theoretically determined by the fluorescence emission spectra of isolated PSI and PSII. In practice, the PSI and PSII fluorescence emission spectra used in SCOPE (i.e., the fixed fluorescence shapes) were measured in a dilute suspension of light-harvesting complexes to avoid (re)absorption artifacts (Pedrós et al., 2010). Previous studies have suggested the measured fluorescence emission spectra of isolated PSI and PSII complexes can be assumed to remain almost unchanged (Franck et al., 2002; Pedrós et al., 2010). Thus, $f_C(\lambda)$ at a specific wavelength ($640 < \lambda < 850 \text{ nm}$) is a

constant, allowing reconstructing broadband SIF at photosystem level from $SIF_{TOT_760_PSII}$. Detailed descriptions of estimating the conversion ratio by using PC1 can be found in the supplementary materials (Text S1). $SIF_{TOT_FULL_PSII}/f_{esc_P-C}$ in Eq. (1) (i.e., $SIF_{TOT_FULL_PSII}$) should have units of $\mu\text{mol m}^{-2} \text{s}^{-1}$, while $SIF_{TOT_760_PSII}$ has units of $\text{mW m}^{-2} \text{nm}^{-1}$, so we also performed the unit conversion when obtaining $SIF_{TOT_FULL_PSII}$:

$$SIF_{TOT_FULL_PSII} = \sum_{\lambda=640}^{850} \left(SIF_{TOT_760_PSII} \times f_c(\lambda) \times \frac{\lambda \times 10^6}{h \times c \times N_A \times 10^3 \times 10^9} \right) \quad (20)$$

where h is the Planck constant ($6.63 \times 10^{-34} \text{ J}\cdot\text{s}$); c is the speed of light ($3 \times 10^8 \text{ m s}^{-1}$); N_A is the Avogadro constant ($6.02 \times 10^{23} \text{ mol}^{-1}$); λ is the wavelength (nm); 10^3 is used to convert milliwatts (mW) to Watts (W); 10^9 is used to convert nanometers (nm) to meters (m) in λ ; 10^6 is used to convert moles (mol) to micromoles (μmol) in N_A .

3.3. Estimation of K_{DF}

In the original MLR model, the ratio between K_D and K_F , K_{DF} , was assumed to be 19 (Gu et al., 2019a). However, its value has been set to around 9 in other studies (Atherton et al., 2016; Porcar-Castell et al., 2006; Zaks et al., 2012). According to its definition, K_{DF} can be estimated from the maximum fluorescence quantum yield of PSII under dark-adapted conditions ($\Phi_{F_{max}}$, Porcar-Castell et al., 2006). Here, $\Phi_{F_{max}}$ was defined as the ratio of the PSII fluorescence emission, obtained from the maximum fluorescence quantum yield in the dark-adapted leaves and presented in photon flux density units ($\mu\text{mol m}^{-2} \text{s}^{-1}$), to the absorbed incident photosynthetic active radiation in PSII. We have:

$$K_{DF} = \frac{1}{\Phi_{F_{max}}} - 1 \quad (21a)$$

$$\Phi_{F_{max}} = \frac{K_F}{K_F + K_D} \quad (21b)$$

$$\Phi_{F_{max}} = \frac{\text{ChlF}_{PSII_{max}}}{\omega \times \text{PAR}_{SP}} \quad (21c)$$

where $\text{ChlF}_{PSII_{max}}$ is the broadband chlorophyll fluorescence flux from PSII, presented in photon flux density units ($\mu\text{mol m}^{-2} \text{s}^{-1}$), which corresponds to the maximum fluorescence quantum yield obtained with fully dark-adapted leaves. PAR_{SP} is the photon flux density of a saturation pulse ($\mu\text{mol m}^{-2} \text{s}^{-1}$), and ω was the product of light absorption efficiency in PSII and the escape probability of fluorescence photons

from the photosystem level to leaf level (Gu et al., 2019a).

To estimate K_{DF} by measuring fluorescence flux, we developed a leaf-level concurrent instrument (Fig. 3) by integrating an LI-6800 portable gas-exchange system (LI-COR Biosciences, Lincoln, Nebraska, USA), a PAM fluorometer (Dual-PAM-100, Heinz Walz GmbH, Effeltrich, Germany), and two QE Pro spectrometers. The gas-exchange system regulated environmental conditions in the leaf chamber, while the PAM fluorometer was used to induce the maximum fluorescence quantum yield obtained with fully dark-adapted samples using the saturation pulse method ($\text{PAR}_{SP} = 10,000 \mu\text{mol m}^{-2} \text{s}^{-1}$). The spectrometers synchronously measured upward and downward fluorescence emission from 670 to 850 nm (ChlF_{max} , $\text{mW m}^{-2} \text{nm}^{-1} \text{sr}^{-1}$) during the initial saturation pulse. The reason for using the 670–850 nm range is explained by Meeker et al. (2021). Details of the process of estimating ω are given in the supporting material (Text S2). Concurrent measurements were conducted on intact and fully developed leaves of winter wheat at the Yangling site, in and around the location of the SIF observations. During the measurements, air relative humidity and flow rate were maintained at 50% and $500 \mu\text{mol s}^{-1}$, respectively. In addition, air temperature (15, 25, and $35 \text{ }^\circ\text{C}$) and CO_2 concentration (200, 400, and 600 ppm) in the leaf chamber were manually set as described in Table 1. ChlF_{max} was converted to $\text{ChlF}_{PSII_{max}}$ by using Eqs. (9a)–(10). To extract PSII ChlF, the coefficients m_1 and m_2 in Eq. (9b) for the other bands were obtained from the PSI and PSII fluorescence emission spectrum used in the SCOPE model (Bacour et al., 2019; van der Tol et al., 2009). Φ_{F0} and Φ_F in Eq. (10) were set to F_0 and F_m measured by

Table 1

Variation in K_{DF} in winter wheat under two different CO_2 concentration and air temperature treatments.

CO_2 (ppm)	T_{air} ($^\circ\text{C}$)	K_{DF}				Means \pm SE ($n = 4$)
200	15	11.5	12.2	11.6	13.1	12.1 ± 0.7
200	25	10.6	11.7	12.8	9.9	11.2 ± 1.3
200	35	11.6	12.4	11.7	11.0	11.7 ± 0.6
400	15	10.9	12.9	11.6	11.8	11.8 ± 0.9
400	25	12.0	11.7	12.0	11.4	11.8 ± 0.3
400	35	11.8	12.3	13.5	11.8	12.3 ± 0.8
600	15	12.5	12.8	10.4	12.5	12.1 ± 1.1
600	25	11.5	11.5	12.8	12.0	12.0 ± 0.6
600	35	11.8	12.4	13.0	13.5	12.7 ± 0.8

There are no significant differences in K_{DF} for the two treatments ($p > 0.05$).

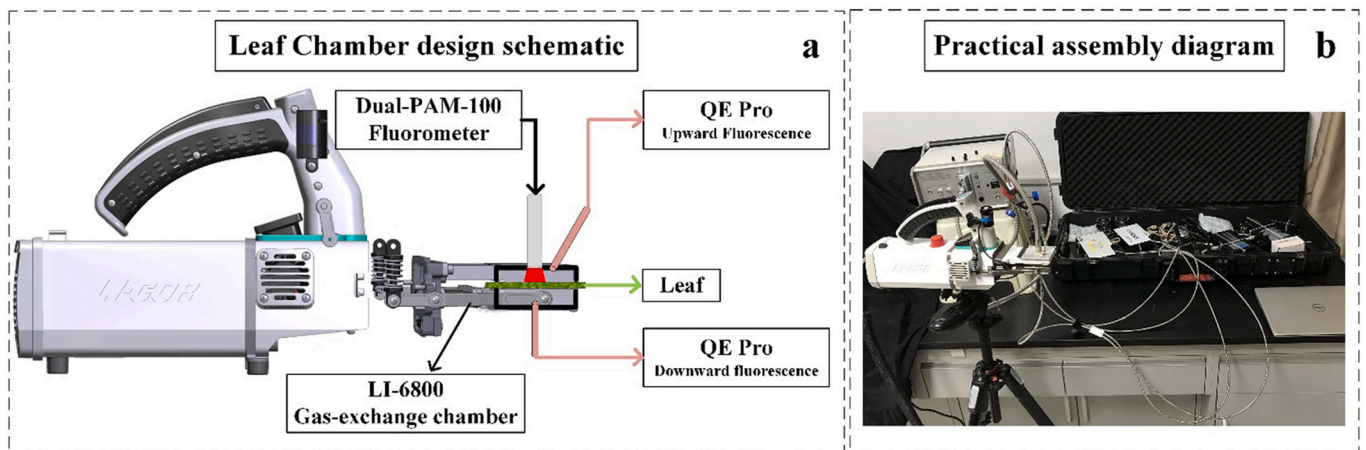


Fig. 3. Schematic of the K_{DF} measurement system. (a) a customized leaf chamber coupled with a pulse-amplitude modulation (PAM) fluorometer and two spectrometers to conduct fluorescence flux measurements induced by a saturation pulse in dark-adapted conditions. The black rectangle indicates that the leaf chamber was painted with black acrylic paint as a light trap, and the red trapezoid represents a saturation light pulse emitting from a PAM fluorometer. (b) a photograph of the K_{DF} measurement system including an LI-6800 gas-exchange chamber (LI-COR Biosciences, Lincoln, Nebraska, USA), a Dual-PAM-100 fluorometer (Dual-PAM-100, Heinz Walz GmbH, Effeltrich, Germany), and two QE Pro spectrometers (Ocean Optics, Dunedin, Florida, USA). (For interpretation of the references to colour in this figure legend, the reader is referred to the web version of this article.)

PAM fluorometry, respectively. Our results showed that K_{DF} varied in a small range between 11.0 and 12.7 (Table 1). Note that Φ_{Fmax} should increase as PAR_{SP} increases. Thus, K_{DF} decreases with increased PAR_{SP} and reaches its minimum value at infinite PAR_{SP} . In other words, K_{DF} should at least be smaller than 11.0. We therefore assumed $K_{DF} = 9$ in this study ($K_D = 0.9$ and $K_F = 0.1$).

3.4. Estimation of Γ^* and C_c

Next, we need to estimate Γ^* and C_c in Eq. (8). Γ^* was estimated as (Katul et al., 2010; Liu et al., 2017):

$$\Gamma^* = 36.9 + 1.18 \times (T_{air} - 25) + 0.036 \times (T_{air} - 25)^2 \quad (22)$$

and C_c could be estimated as (Wu et al., 2019):

$$C_c = C_i - \frac{A_{net}}{g_m} \quad (23)$$

where C_i is intercellular CO_2 partial pressure (μbar); A_{net} is net CO_2 assimilation rate ($\mu\text{mol m}^{-2} \text{s}^{-1}$); g_m is mesophyll conductance to CO_2 ($\text{mol m}^{-2} \text{s}^{-1} \text{bar}^{-1}$). As a simplification, g_m was assumed to be infinite (van der Tol et al., 2009) and, consequently, C_c was considered to be equal to C_i .

An iterative process was used to estimate C_i , as described below:

(1) calculate the initial C_i as a constant fraction of C_a :

$$C_i = 0.7 \times C_a \quad (24)$$

where C_a is the ambient air CO_2 partial pressure (μbar) and the default ratio of C_i ; C_a was set to 0.7 for C3 wheat (Wu et al., 2019).

(2) estimate A_{net} using the initial C_i :

$$A_{net} = \min(A_C, A_J) - R_d \quad (25)$$

where both A_C and A_J are from Eq. (14); R_d is dark respiration ($\mu\text{mol m}^{-2} \text{s}^{-1}$) and calculated as $R_d = 0.015 \times V_{cmax}$ (Collatz et al., 1991); V_{cmax} is the maximum carboxylation rate ($\mu\text{mol m}^{-2} \text{s}^{-1}$) which is calculated as (Bonan, 1995; Chen et al., 1999):

$$V_{cmax} = V_{cmax25} \times 2.4^{(T_{air}-25)/10} \times f(T_{air}) \times f(N) \quad (26a)$$

$$f(T_{air}) = \frac{1}{1 + \exp\left(\frac{-22000 + 710 \times (T_{air} + 273)}{R_{gas} \times (T_{air} + 273)}\right)} \quad (26b)$$

$$f(N) = \frac{N}{N_m} \quad (26c)$$

where V_{cmax25} is the maximum carboxylation rate at 25 °C assumed to be $60 \mu\text{mol m}^{-2} \text{s}^{-1}$ for winter wheat (Bacour et al., 2019); R_{gas} is the molar gas constant ($8.3143 \text{ m}^3 \text{ Pa mol}^{-1} \text{ K}^{-1}$); N and N_m are the leaf nitrogen content (1.2%, Kimball et al. (1997)) and the maximum nitrogen content (1.5%, Bonan (1995)), respectively.

(3) Estimate the stomatal conductance for CO_2 (G_c , $\text{mol m}^{-2} \text{s}^{-1}$) using a modified Ball–Woodrow–Berry model (Wang and Leuning, 1998)

$$G_s = G_o + \frac{a \times f_w \times A_{net}}{C_s \times (1 + VPD/D_o)} \quad (27a)$$

$$G_c = 0.64 \times G_s \quad (27b)$$

where G_o is the residual conductance ($\text{mol m}^{-2} \text{s}^{-1}$), assumed to be 0.01 (Wang and Leuning, 1998); C_s is the CO_2 concentration at the leaf surface ($\mu\text{mol mol}^{-1}$), assumed to be the product of $a/(a-1)$ and C_i ; a is a parameter related to C_i , assumed to be 11.0 (Wang and Leuning, 1998); D_o (kPa) is an empirical parameter related to stomatal sensitivity to VPD, assumed to be 1.5 (Wang and Leuning, 1998); f_w is a parameter related to soil moisture, which is estimated by the soil water content at the field capacity and at the wilting point and the measured SWC (Wang

and Leuning, 1998); G_s is the stomatal conductance for water vapor ($\text{mol m}^{-2} \text{s}^{-1}$); 0.64 is a factor to convert the molecular diffusivity of water vapor to CO_2 (Ju et al., 2006).

(4) Calculate a new C_i based on the CO_2 diffusion model (Ju et al., 2006):

$$C_i = C_a - \frac{A_{net}}{G_c} \quad (28)$$

(5) Iterate (Eqs. (24)–(28)) until the estimated C_i is stable, i.e. when the difference in C_i between two successive iterations is less than 0.1 ppm. C_i from the last iteration (Eq. (28)) represents the final value used in the SIF-based photosynthesis model (Eq. (8)).

4. Results

4.1. Temporal patterns of the measurements

The seasonal patterns of the required inputs for our model (air temperature (T_{air}), incoming PAR, direction reflectance at 680 and 755 nm (R_{680} , R_{755}), and TOC SIF at 760 nm (SIF_{TOC,760}) and measured GPP (GPP_{EC}) are shown in Fig. 4.

T_{air} maintained a generally increasing trend during the study period, increasing from below 0 °C in late December to more than 25 °C in early June, with the highest daily mean T_{air} being approximately 33.8 °C on 07 June 2021 (Fig. 4a). Several cold spells were also observed. For example, on 25 February 2021 the daily mean temperature fell to 4.8 °C (black dashed line in Fig. 4a). The time series of incoming PAR increased similarly to T_{air} , but its seasonal trend was less pronounced: maximum PAR increased from 565 $\mu\text{mol m}^{-2} \text{s}^{-1}$ in December 2020 to 1280 $\mu\text{mol m}^{-2} \text{s}^{-1}$ in June 2021 (Fig. 4b).

R_{680} decreased as the fractional vegetation cover increased and it appeared saturated with a mean value of around 0.03 after March 2021 (Fig. 4c), a result of R_{680} of vegetation being lower than that of soil. In contrast, R_{755} exhibited a different seasonal dynamic: it increased from 0.2 in mid-February to 0.4 in late March due to the enhanced scattering effect in the NIR band, and it started to decrease in mid-April as a result of crop yellowing (Fig. 4c). NDVI, being a function of both R_{680} and R_{755} , remained relatively stable with a mean value around 0.4 until mid-January, showed a significant increase at the most intensive plant-growth stage in early spring, and appeared saturated at a value of 0.95 from mid-March through harvesting (Fig. 4d). As expected, NDVI remained insensitive to short-term changes in T_{air} and day-to-day variability in incoming PAR (Fig. 4d). Both NIRv and f_{APAR} were obtained from reflectance: the seasonal trajectory of NIRv was more similar to R_{755} (Fig. 4e), while that of f_{APAR} more closely resembled the magnitude and timing of NDVI trend (Fig. 4f).

SIF_{TOC,760} not only exhibited a strong seasonal pattern as stems and leaves developed, with a rapid increase from 0.1 ($\text{mW m}^{-2} \text{nm}^{-1} \text{sr}^{-1}$) in the winter to higher than 1.0 ($\text{mW m}^{-2} \text{nm}^{-1} \text{sr}^{-1}$) in the summer, but also had hour-to-hour variations, driven mainly by incoming PAR, leading to strong fluctuations in March–June (Fig. 4g). GPP_{EC} generally followed the temporal pattern of SIF_{TOC,760}: its values increased substantially from about 5 $\mu\text{mol m}^{-2} \text{s}^{-1}$ in mid-January to more than 30 $\mu\text{mol m}^{-2} \text{s}^{-1}$ at the end of March; it then showed strong variability in the range 10 to 35 $\mu\text{mol m}^{-2} \text{s}^{-1}$ throughout the rest of the growing season (Fig. 4h). Compared to the reflectance-based indices, both SIF_{TOC,760} and GPP_{EC} had a much higher sensitivity to changing environmental conditions, showing dramatic decreases when cold spells occurred (Fig. 4g–h).

4.2. The performance of the model for estimating GPP

Fig. 5 shows the correlation coefficient (R^2), root-mean-squared error (RMSE) and relative root-mean-square error (rRMSE) between

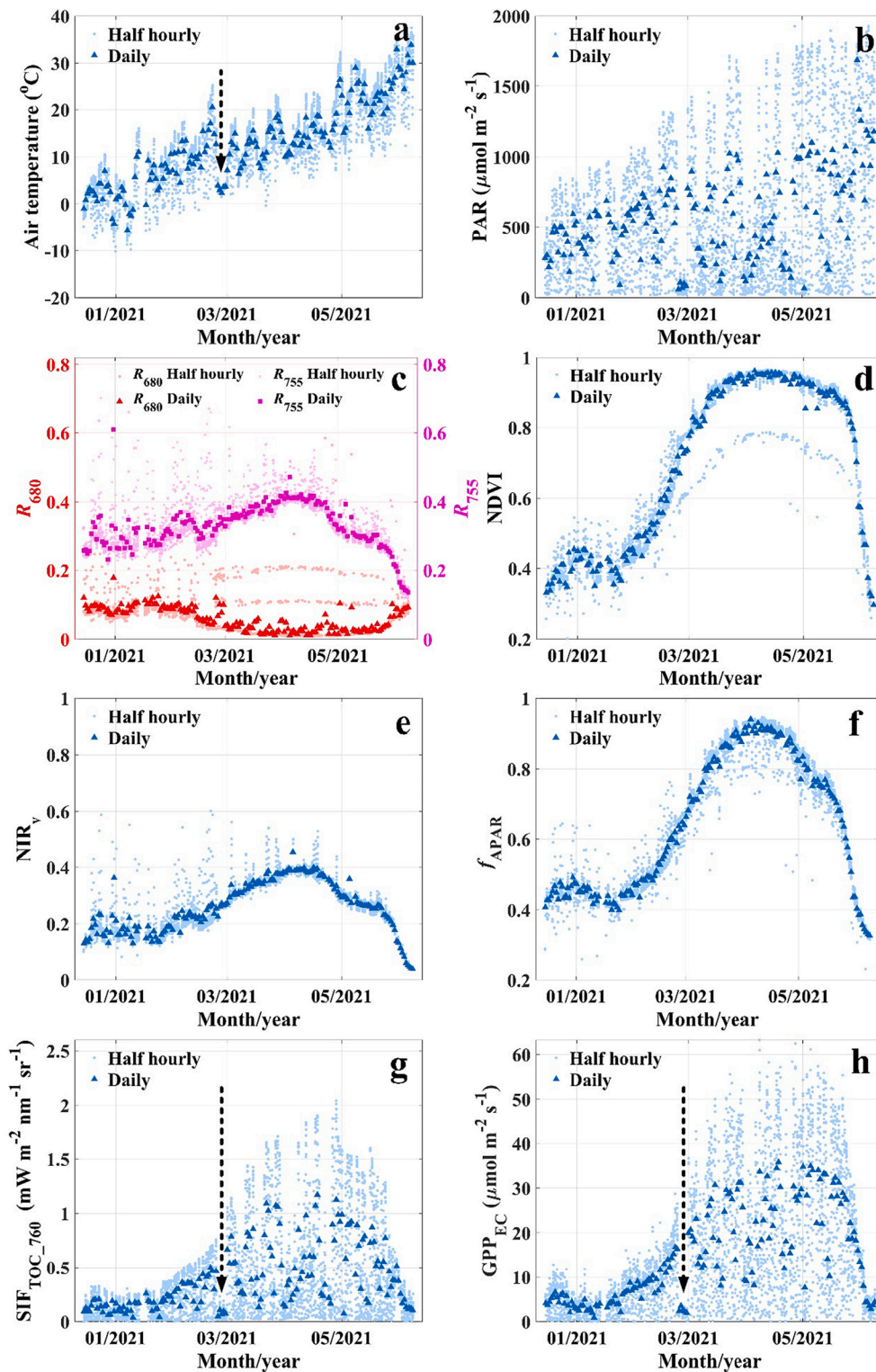


Fig. 4. Seasonal variations of T_{air} ($^{\circ}\text{C}$, a), PAR ($\mu\text{mol m}^{-2} \text{s}^{-1}$, b), R_{680} (c), R_{755} (c), NDVI (d), NIR_v (e), f_{APAR} (f), $\text{SIF}_{\text{TOC},760}$ ($\text{mW m}^{-2} \text{nm}^{-1} \text{sr}^{-1}$, g), and GPP_{EC} ($\mu\text{mol m}^{-2} \text{s}^{-1}$, h). Light-blue circles indicate half-hourly data ($N_{\text{half, hourly}} = 3394$), and blue triangles represent daily mean values ($N_{\text{daily}} = 171$). Black dashed lines (a, g, and h) indicate the cold spell that occurred on 25 February 2021. T_{air} and PAR represent air temperature and photosynthetically active radiation, respectively. NDVI is the normalized difference vegetation index. f_{APAR} is the photosynthetically active radiation absorption efficiency. R_{680} and R_{755} are directional reflectances at 680 nm and 755 nm, respectively. NIR_v is the product of NDVI and R_{755} . $\text{SIF}_{\text{TOC},760}$ is top of canopy SIF radiance at 760 nm. GPP_{EC} is gross primary production estimated from flux data at the study site. (For interpretation of the references to colour in this figure legend, the reader is referred to the web version of this article.)

observed GPP (GPP_{EC}) and simulated GPP (GPP_{SIF}) from Eq. (8) at both a half hourly (Fig. 5a) and daily (Fig. 5b) time step. Overall, the proposed model explains 85% of variance ($\text{RMSE} = 5.62 \mu\text{mol m}^{-2} \text{s}^{-1}$ and $\text{rRMSE} = 9.10\%$) in half-hourly GPP (Fig. 5a), and its performance improves at the longer time step: GPP_{SIF} accounts for 91% of the variability ($\text{RMSE} = 3.25 \mu\text{mol m}^{-2} \text{s}^{-1}$ and $\text{rRMSE} = 8.69\%$) in the daily GPP_{EC} time series (Fig. 5b). Both regression lines have a slope close to 1.0, indicating that GPP_{SIF} was very similar to GPP_{EC} . We also made a direct comparison

with the commonly used linear regression approach that scaled $\text{SIF}_{\text{TOC},760}$ to GPP_{EC} as shown in Fig. S5. Although $\text{SIF}_{\text{TOC},760}$ and GPP_{EC} were correlated with overall $R^2 > 0.82$, the saturation of GPP_{EC} at high $\text{SIF}_{\text{TOC},760}$ values was also observed ($> 1.4 \text{mW m}^{-2} \text{nm}^{-1} \text{sr}^{-1}$ for half-hourly data, Fig. S5a; $> 0.9 \text{mW m}^{-2} \text{nm}^{-1} \text{sr}^{-1}$ for daily data, Fig. S5b). In contrast, GPP_{SIF} estimated by the proposed model displayed a strong linear relationship with the tower GPP_{EC} even at high $\text{SIF}_{\text{TOC},760}$ values as shown in Fig. 5. To assess the impact of the choice of K_{DF} value on the

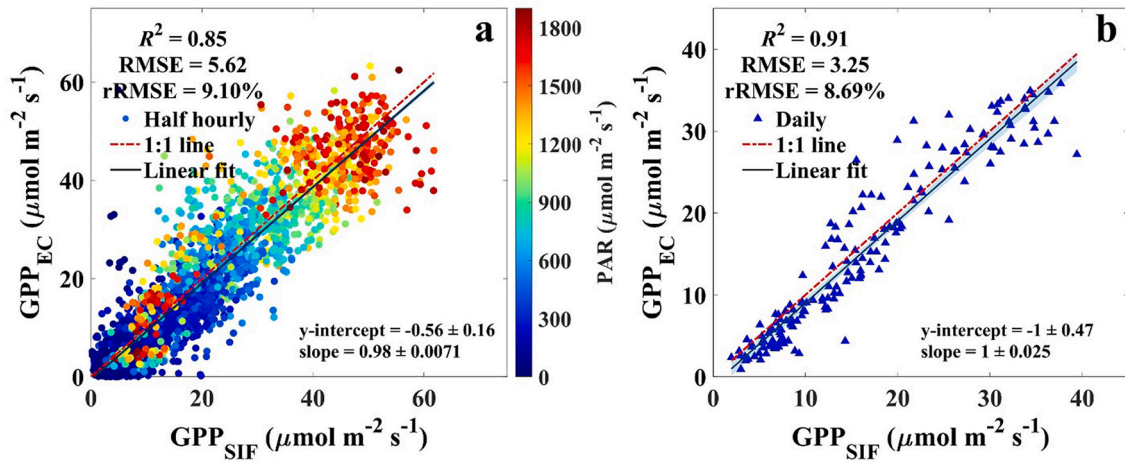


Fig. 5. Comparison of observed and simulated GPP (GPP_{EC} versus GPP_{SIF} , $\mu\text{mol m}^{-2} \text{s}^{-1}$) at half-hourly (a) and daily (b) scales. The colors of the points in (a) represent the different values of PAR. R^2 is the coefficient of determination, RMSE is the root-mean-square error ($\mu\text{mol m}^{-2} \text{s}^{-1}$), and rRMSE is the relative root-mean-square error (%). All the datasets have a half-hourly time step. Data with low PAR ($< 20 \mu\text{mol m}^{-2} \text{s}^{-1}$) were excluded from the analysis.

performance of the proposed model (Eq. (8)), we performed a sensitivity analysis of GPP_{SIF} to K_{DF} as shown in Fig. S6. R^2 between GPP_{SIF} and GPP_{EC} remained a constant value at 0.849 as K_{DF} varied from 9 to 19. In contrast, the RMSE between GPP_{SIF} and GPP_{EC} increased from 5.62 to $23.46 \mu\text{mol m}^{-2} \text{s}^{-1}$ (Fig. S6). It confirmed that K_{DF} had a significant impact on the accuracy of GPP estimation.

The derivation of $f_{esc,L-C}$ (Eq. (17)) requires a black-soil simplification (Yang et al., 2020) which is only valid for either dense canopy or black soil conditions. NDVI was introduced to reduce soil background contamination (Zeng et al., 2019). To examine how this soil background effect and the inclusion of NDVI may affect the performance in estimating GPP, it was desirable to assess variations in SIF-GPP correlations under different LAI values. Because LAI was not measured at the study site, we used NDVI as a surrogate for plant canopy structure. All the required inputs and GPP_{EC} were separated into two groups according to NDVI values: (1) low: $NDVI \leq 0.60$, and (2) high: $NDVI > 0.60$ (Fig. 4d). Incoming PAR and T_{air} also play the important roles in the proposed model, so we assessed the performance of the model in response to variations in these two meteorological variables. We set thresholds of $600 \mu\text{mol m}^{-2} \text{s}^{-1}$ in PAR and 20°C in T_{air} . Because both PAR and T_{air} were closely correlated with plant canopy growth, we only analyzed data with $NDVI > 0.60$ to reduce any possible influence of the canopy structure (Table 2).

We found that the performance of the proposed model decreased for sparse canopies. The results are shown in Table 2. GPP_{SIF} accounted for 58% of the variance in GPP_{EC} ($RMSE = 3.23 \mu\text{mol m}^{-2} \text{s}^{-1}$ and $rRMSE = 11.56\%$) when NDVI was lower than 0.60. The dense plant canopy tended to improve the performance of the proposed model in estimating GPP: GPP_{SIF} determined more than 80% of the variance in half-hourly

Table 2

The effects of NDVI (a surrogate for plant canopy structure), air temperature (T_{air} , $^\circ\text{C}$), and PAR ($\mu\text{mol m}^{-2} \text{s}^{-1}$) on the performance of the model in predicting GPP ($\mu\text{mol m}^{-2} \text{s}^{-1}$). R^2 is the coefficient of determination, RMSE is the root-mean-square error, and rRMSE is the relative root-mean-square error. N is the number of available half-hourly observations. All the datasets have a half-hourly time step. Data with low PAR ($< 20 \mu\text{mol m}^{-2} \text{s}^{-1}$) were excluded from the analysis.

	NDVI ≤ 0.60	NDVI > 0.60	PAR (NDVI > 0.60)		T_{air} (NDVI > 0.60)	
			≤ 600	> 600	≤ 20	> 20
R^2	0.58	0.80	0.65	0.58	0.84	0.76
RMSE	3.23	6.36	5.06	7.76	5.56	7.97
rRMSE	16.56	10.30	14.08	14.76	9.13	12.95
N	988	2261	1293	968	1602	659

GPP ($RMSE = 6.36 \mu\text{mol m}^{-2} \text{s}^{-1}$ and $rRMSE = 10.30\%$) when NDVI was higher than 0.60. High PAR exerted a negative impact on the correlation between GPP_{EC} and GPP_{SIF} , GPP_{SIF} explained nearly 70% of the variance in GPP_{EC} ($RMSE = 5.06 \mu\text{mol m}^{-2} \text{s}^{-1}$ and $rRMSE = 14.08\%$) in the low PAR group. But their correlation was weakened under high PAR: R^2 decreased to 0.58 ($RMSE = 7.76 \mu\text{mol m}^{-2} \text{s}^{-1}$ and $rRMSE = 14.76\%$). Compared with PAR, T_{air} had a limited negative influence on the predictive power of the model: the simulated GPP determined 84% of the observed GPP variability ($RMSE = 5.56 \mu\text{mol m}^{-2} \text{s}^{-1}$ and $rRMSE = 9.13\%$) in the low T_{air} group; R^2 fell to 76% ($RMSE = 7.97 \mu\text{mol m}^{-2} \text{s}^{-1}$ and $rRMSE = 12.95\%$) in the high T_{air} group.

4.3. The variations in f_{PSII} and $f_{esc,P-C}$

The conversion from $SIF_{TOC,760}$ to $SIF_{TOT,FULL,PSII}$ is dependent on three important variables: f_{PSII} , $f_{esc,P-C}$, and $f_C(\lambda)$. In this section, we examine the seasonal patterns of f_{PSII} and $f_{esc,P-C}$. $f_C(\lambda)$ is constant over time and so not included in this analysis. f_{PSII} showed an increasing seasonal pattern before March, rising from 0.4 in the winter to greater than 0.5 in early spring, but it appeared to remain at around 0.5 for the rest of the growing season (Fig. 6a). We found that f_{PSII} was positively associated with T_{air} when $T_{air} < 15^\circ \text{C}$ (Fig. 6b), which led to the generally increasing trend in f_{PSII} from winter to summer. However, f_{PSII} exhibited a saturation behavior at higher values of T_{air} (Fig. 6b), explaining the fact that daily mean f_{PSII} remained stable in May and June while T_{air} still had an increasing trend (Fig. 6a). The relationship between f_{PSII} and PAR was more nonlinear: f_{PSII} was negatively correlated with PAR when PAR was less than $300 \mu\text{mol m}^{-2} \text{s}^{-1}$, but became less responsive as PAR continued to increase (Fig. 6c). We observed that the timing and magnitude of the rapid increases in f_{PSII} closely corresponded with abrupt drops in PAR, confirming the important role of PAR in regulating short-term variations in f_{PSII} (Fig. 6a).

We also examined seasonal changes in $f_{esc,P-C}$: $f_{esc,P-C}$ had modest fluctuations in the range between 0.2 and 0.4 before mid-February, thereafter remaining relatively constant until harvesting, with an average value of around 0.4 (Fig. 6d). $f_{esc,P-C}$ is determined by the ratio of NIR_V and f_{PAR} (Eq. (16)), both of which exhibited similar seasonal trajectories, with a rapid increase in early spring followed by a rough plateau before harvest (Fig. 4e–f). A consequence of the offset between their seasonal variations was the relatively stable trend of $f_{esc,P-C}$ after March. We found that $f_{esc,P-C}$ increased linearly with NDVI when $NDVI < 0.6$ (Fig. S3), but tended to saturate when the plant vegetation canopy was dense ($NDVI > 0.6$) (Fig. S3), highlighting the need to account for the interaction between understory and overstory for relatively sparse

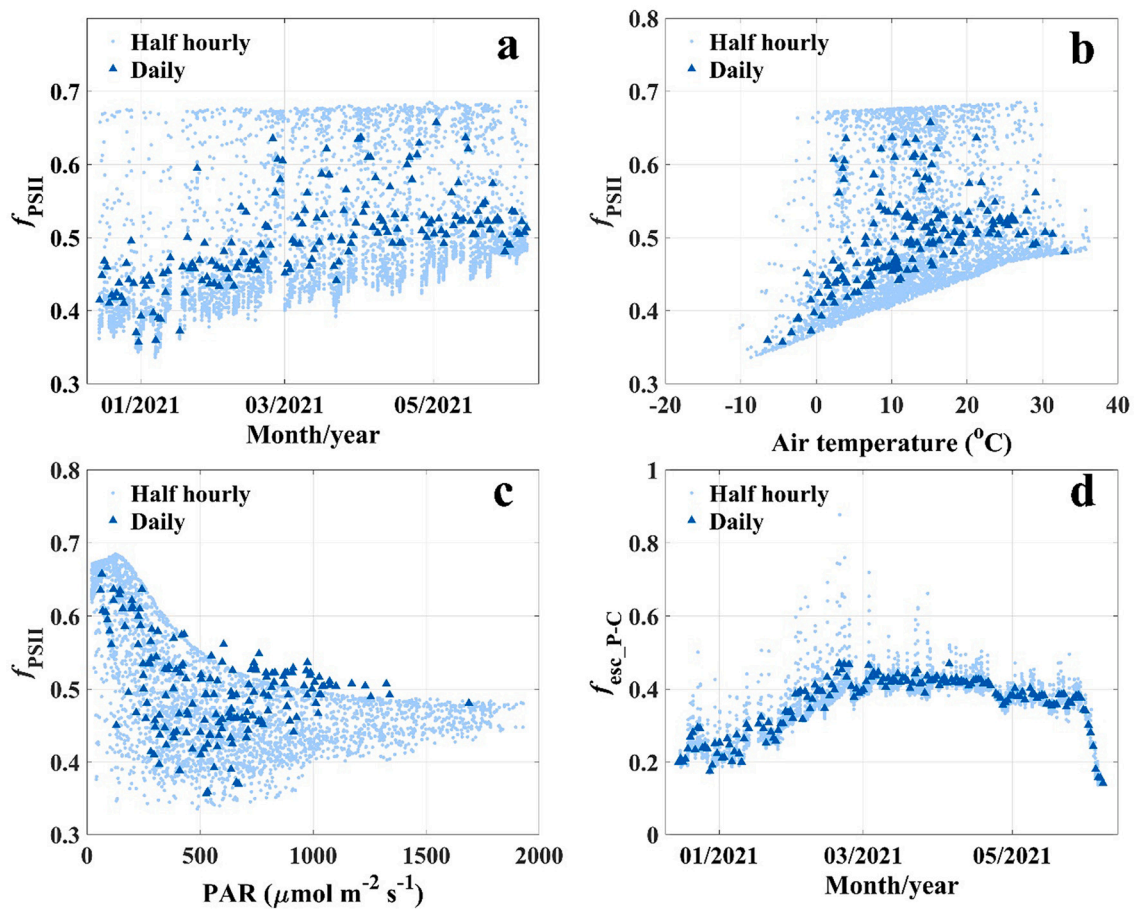


Fig. 6. Seasonal dynamics of the contribution of PSII fluorescence to TOC SIF (f_{PSII}) for the 2021 growing season (a), f_{PSII} for T_{air} (b), f_{PSII} for PAR (c), and the SIF escape probability from the photosystem level to the canopy at 760 nm ($f_{\text{esc_P-C}}$, d) at half-hourly (light-blue dots) and daily scales (blue triangles). (For interpretation of the references to colour in this figure legend, the reader is referred to the web version of this article.)

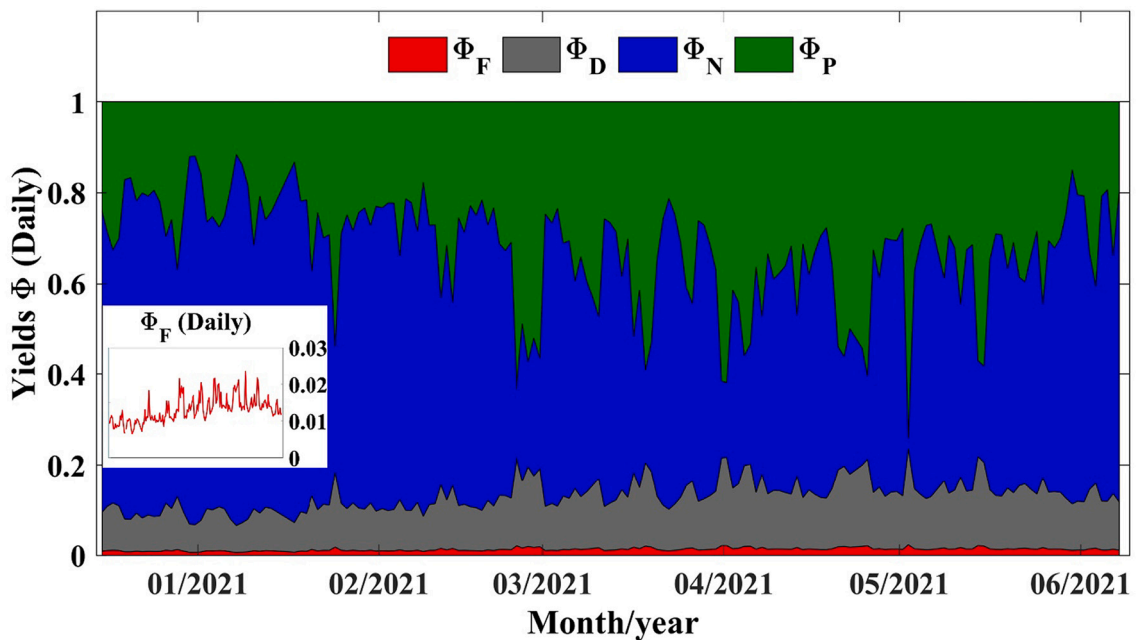


Fig. 7. Seasonal variations in the simulated quantum yields (Φ) for the different pathways: fluorescence (Φ_{F} , red), nonradiative decay (Φ_{D} , grey), nonphotochemical quenching (Φ_{N} , blue), and photosynthesis (Φ_{P} , green). The inset panel illustrates the seasonal pattern of Φ_{F} . These results were derived from Eq. (S7) in Text S3. (For interpretation of the references to colour in this figure legend, the reader is referred to the web version of this article.)

canopies.

4.4. Variations in the quantum yields

In addition to Φ_p (Eq. (14)), we were able to simulate the other three quantum yields: the fluorescence yield (Φ_f), the non-photochemical quenching yield (Φ_n), and the constitutive heat dissipation (Φ_d), from the rate constants (K_p , K_f , K_n , and K_d ; Text. S3). Note that we should have: $\Phi_p + \Phi_f + \Phi_n + \Phi_d = 1$. Because K_f and K_d remained constant, the dynamics of these four quantum yields are mostly related to the interaction between K_p and K_n . K_p showed a slight decrease with increasing T_{air} , from 2.4 in the winter to 2.2 in the summer (Fig. S4). In contrast, the same increase in T_{air} caused a much greater reduction in K_n , from approximately 11.9 to 3.8 (Fig. S4). The different sensitivity of K_p and K_n to variations in T_{air} explains the seasonal increase in Φ_p , especially from March to April, when T_{air} was increasing (Fig. 7). Also, because both K_p and K_n were negatively correlated with T_{air} , Φ_f and Φ_d both increased from winter towards early summer (Fig. 7). K_p was negatively correlated to PAR while K_n was positively correlated (Text S3 & Fig. S4), which led to a decrease in Φ_p from early summer onwards as PAR continually increased (Fig. 7). We observed steep increases in Φ_p in response to the sudden drops in PAR which occur from February 2021 onwards (Figs. 3b & 6).

Being negatively correlated with Φ_p , Φ_n had an opposite seasonal pattern to Φ_p : decreasing from late winter to spring and increasing from late-May through harvesting (Fig. 7). Due to the canceling effect of Φ_p and Φ_n , we also observed that the sum of Φ_p and Φ_n remained, on the whole, stable, and that seasonal variations in Φ_f and Φ_d were also limited (Fig. 7), only ranging from 0.010 to 0.024, and 0.090 to 0.212, respectively (Fig. 7).

5. Discussion

Three steps were involved in obtaining $SIF_{TOT,FULL,PSII}$: (1) extracting the PSII contribution of TOC SIF observations (f_{PSII}), (2) downscaling from canopy level to photosystem level ($f_{esc,P-C}$), and (3) converting from narrowband to broadband SIF emissions at the photosystem level ($f_C(\lambda)$). Although nonlinear functions were introduced to parameterize f_{PSII} (Eq. (9b)) and $f_{esc,P-C}$ (Eq. (17)), we found that $SIF_{TOC,760}$ was strongly related with $SIF_{TOT,FULL,PSII}$ with $R^2 > 0.95$, suggesting that it may be possible to convert $SIF_{TOC,760}$ into $SIF_{TOT,FULL,PSII}$ with a simple function. Their strong correlation observed here resulted from: (1) f_{PSII} saturated with increasing T_{air} and PAR and the thresholds for winter wheat were relatively low (approximately 15 °C for T_{air} and 300 $\mu\text{mol m}^{-2} \text{s}^{-1}$ for PAR), and (2) $f_{esc,P-C}$ also saturated at a relatively low NDVI value (≈ 0.6). Taken together, both f_{PSII} and $f_{esc,P-C}$ were rather stable (approximately 0.5 and 0.4, Fig. 6a & d) during the period when winter wheat had its highest carbon sequestration rate (March–June, Fig. 4h). However, a variety of physiological and structural factors may also affect not only these thresholds but also the saturation levels of f_{PSII} and $f_{esc,P-C}$. More experimental and theoretical work is required to investigate this possibility. For example, as our study site was irrigated, we were unable to fully examine any potential variations in f_{PSII} under conditions of high water stress. Also, $f_{esc,P-C}$ may exhibit more nonlinear behavior for heterogeneous canopies (Yang et al., 2020), such as forests.

The contribution of PSII fluorescence to TOC SIF observations relies on the accuracy of ϵ . In the present approach, ϵ was modeled as a function of Φ_p and K_n (Eqs. (10) and (11), and K_f and K_d were constants), and their parameterization only took T_{air} and PAR into account, potentially leading to poor performance in representing the impacts of other factors including chlorophyll concentration (Gitelson et al., 1998), drought stresses (van der Tol et al., 2014), and seasonal changes in both photosystems (Porcar-Castell et al., 2014). More importantly, the contribution of PSII fluorescence in the red bands (up to 100%) was significantly different from that in the near-infrared bands (down to 50%) (Franck et al., 2002; Palombi et al., 2011; Pfündel et al., 2013). For

example, Pfündel (2021) proposed a practical approach to separately estimate f_{PSII} at the red (<700 nm) and near-infrared bands (>700 nm), and showed that the contribution of PSII fluorescence was 86% and 55% for these two spectral regions, respectively. Considering that the proportion of PSII fluorescence in the red region was typically larger than that in the NIR (Franck et al., 2002; Palombi et al., 2011), f_{PSII} estimated from broadband fluorescence from PSII (33.6–68.6%, Eq. (9b)) may overestimate the contribution of PSII in SIF_{760} . Ideally, f_{PSII} specifically measured or estimated for the near-infrared region should be used to extract PSII fluorescence from SIF_{760} . More measurements will be needed to enable the characterization of f_{PSII} and fluorescence-derived parameters across various vegetation types and environmental conditions in future studies (Porcar-Castell et al., 2021).

We showed that the role of q_L and Φ_{pmax} in the MLR model could be replaced by Φ_p and NPQ (Eq. (7)). These two expressions were identical under the framework of the lake model (Kramer et al., 2004). The minimum fluorescence yield in light-adapted conditions (F_0') was a vital parameter in determining q_L which should be measured in a dark interval with a short pulse of far-red light (Kramer et al., 2004). Thus, measurements of q_L can only be obtained in a dark leaf chamber under artificial light conditions. The complicated measurement procedures may limit the development of a predictive model for q_L (Gu et al., 2019a). In contrast, the estimation of Φ_p and NPQ require F_m' , F_s , and F_m , which can be measured by a PAM fluorometer in field conditions (Porcar-Castell, 2011). Various models have been developed to predict canopy Φ_p and NPQ as functions of environmental factors (Bacour et al., 2019; Lee et al., 2015; Rosema et al., 1998; van der Tol et al., 2014). However, it should be noted that predicting Φ_p may be as hard as predicting carbon assimilation itself because both are affected by the same environmental factors and the same biological processes. Theoretically, expressing the relationship between SIF and GPP in terms of q_L rather than NPQ may be advantageous because NPQ contains many mechanisms which are not well understood (Gu et al., 2019a). Considering the importance of q_L in correlating SIF and GPP, and it being less complicated than Φ_p and NPQ in terms of mechanisms, q_L should be further investigated under various environmental conditions and for different species to develop a predictive model of q_L in future research.

The current parametric model of K_n (Eq. (12)) accounts for the impacts of PAR, T_{air} , and Φ_p ; Φ_p was estimated by the photosynthesis model using PAR, T_{air} , and V_{cmax25} as the inputs (Eq. (14)) (Bacour et al., 2019; van der Tol et al., 2014; Yin and Struik, 2009). However, the models for K_n and Φ_p may not respond reasonably to stresses caused by factors other than light and heat, such as droughts or the photoinhibition of reaction centers. Moreover, the parameters in the K_n model (i.e., the parameters a-f in Eq. (12)) were calibrated using leaf-scale fluorescence measurements for eggplant (*Solanum melongena*), needleleaf forest (*Pinus sylvestris*), and several broadleaf plants (*Quercus ilex* L., *Celtis australis* L., *Pistacia terebinthus* L.) (Flexas et al., 2002; Porcar-Castell, 2011). These parameters may result in uncertainties in estimating NPQ and the contribution of PSII fluorescence for winter wheat. Although the good performance of the optimized parametric K_n model was demonstrated in Bacour et al. (2019), more measurements would be required to improve the performance of K_n model for different species. With the exception of the environmental factors, V_{cmax25} is the most crucial parameter that could indirectly impact Φ_p (Kattge and Knorr, 2007; Yin and Struik, 2009). The constant value of V_{cmax25} used in this study (60 $\mu\text{mol m}^{-2} \text{s}^{-1}$) may also lead to uncertainties in the estimation of GPP.

Last, but not least, we were not able to explicitly consider the vertical variability of Φ_p , NPQ, and thus the photosynthetic CO_2 rate within different layers of the canopy. For example, Φ_p (Eq. (14)) in sunlit leaves (high light and high leaf temperature) is lower than in shaded leaves (low light and low leaf temperature), but NPQ (Eq. (12)) is higher in sunlit leaves (high light and high leaf temperature) than in shaded leaves (low light and low leaf temperature). Therefore, it is important that in future research the canopy should be divided into shaded and sunlit components (Qiu et al., 2019) and the photosynthetic parameters (e.g.,

Φ_P and NPQ) quantified for each component.

6. Conclusion

Our study provides a mechanistic framework that can be used to directly estimate not only photosynthetic CO_2 assimilation but also the key information relevant to heat dissipation, PSII contribution, PSII photochemical efficiency, conversion from narrowband into broadband SIF, and the escape ratio of SIF photons. Our model was developed from the MLR model by replacing q_L and $\Phi_{P_{\max}}$ in the original formulation with Φ_P and NPQ, modeled as functions of environmental conditions at the canopy scale. Without relying on statistical regression, the estimated GPP from our model compared well with measurements of flux at a winter-wheat study site, with high R^2 and low RMSE/rRMSE. We also showed that a simple function may be used to represent the overall impact of PSII contribution, conversion to broadband SIF, and escape ratio on predicting GPP during the period of peak photosynthetic activity. This approach may significantly simplify the application of the proposed model at regional or global scales. More experiments are required to fully assess the current parameterizations over a wide range of vegetation species under a variety of environmental conditions. Our findings will allow the community to move on from using statistical models with tuned parameters to using a theory-derived model with more meaningful parameters, providing a step forward in the modeling of the carbon cycle.

Author statement

Zhunqiao Liu: Conceptualization, Methodology, Investigation, Data curation, Writing - original draft, Funding acquisition. Feng Zhao:

Methodology. Xinjie Liu: Methodology. Qiang Yu: Supervision, Resources. Xiongbiao Peng: Investigation, Data curation. Yunfei Wang: Methodology, Data curation. Huanjie Cai: Resources. Xiaoliang Lu: Conceptualization, Methodology, Data curation, Writing - review & editing, Supervision, Funding acquisition, Project administration.

Declaration of Competing Interest

The authors declare that they have no known competing financial interests or personal relationships that could have influenced the work reported in this paper.

Acknowledgments

The authors would like to thank the three anonymous reviewers for their valuable comments and suggestions. The research was supported by the National Natural Science Foundation of China (Grant No. 41901293 to Z.L., 42071328 to X.L., and 41771382 to F.Z.), the China Postdoctoral Science Foundation (Grant No. 2019M663828 to Z.L.), and the Chinese Universities Scientific Fund (24520212452021125 to X.L.). We thank Juan Xie (Horticulture Science Research Center at College of Horticulture, Northwest A&F University, Yangling, China) and Jianchu Zhu (Crop Biology Innovation Center at College of Agronomy, Northwest A&F University, Yangling, China) for their technical support in leaf level fluorescence data collection. The authors gratefully thank Dr. Christiaan van der Tol for providing the SCOPE code and Dr. Alistair Culf for helping with English editing and proofreading. Data and source codes used in this study are available at <https://github.com/luxiaoliaongnwafu/SIF2GPP>.

Appendix A. Definitions and methods for the nomenclature used in this study

Symbols	Definition	Method
GPP_{EC}	Gross primary productivity based on EC observations	Observed
$\text{SIF}_{\text{TOC},760}$	Top-of-canopy (TOC) SIF at 760 nm	Observed
$\text{SIF}_{\text{TOC},760,\text{PSII}}$	Contribution of PSII to TOC SIF at 760 nm	Eq. (9a)
$\text{SIF}_{\text{TOT},760,\text{PSII}}$	Total SIF emitted from all leaves in the canopy at photosystem level at 760 nm	Eq. (15)
$\text{SIF}_{\text{TOT},\lambda,\text{PSII}}$	Total SIF emitted from all leaves in the canopy at photosystem level at a given wavelength λ ($640 \leq \lambda \leq 850$ nm).	Eq. (S5)
$f_c(\lambda)$	The conversion ratio of $\text{SIF}_{\text{TOT},760,\text{PSII}}$ to $\text{SIF}_{\text{TOT},\lambda,\text{PSII}}$ at a given wavelength λ ($640 \leq \lambda \leq 850$ nm).	Eq. (S5), Eq. (20)
$\text{SIF}_{\text{TOT},\text{FULL},\text{PSII}}$	Broadband total (all leaves in the canopy) SIF flux density emitted by PSII	Eq. (20)
f_{PSII}	PSII contribution to $\text{SIF}_{\text{TOC},760}$	Eq. (9b)
ϵ	A factor representing the contribution from PSII fluorescence	Eq. (10)
$f_{\text{esc},\text{L-C}}$	The probability of a fluorescence photon escaping from leaf level to canopy level	Eq. (16)
$f_{\text{esc},\text{P-C}}$	The probability that a SIF photon escapes from the PSII light reactions to the top of the canopy	Eq. (17)
f_{APAR}	Photosynthetically active radiation absorption efficiency	Eq. (18)
K_D	The rate constant for constitutive heat loss	0.9
K_F	The rate constant for fluorescence emission	0.1
K_{DF}	The ratio between K_D and K_F	9
K_P	The rate constant for photochemical quenching	Eq. (5)
K_N	The rate constant for regulated energy-dependent heat dissipation	Eq. (12)
Φ_P	The quantum yield of photochemical quenching in PSII	Eq. (14)
Φ_D	The quantum yield of constitutive heat dissipation	Eq. (S7b)
Φ_N	The quantum yield of regulated heat dissipation	Eq. (S7c)
Φ_F	The quantum yield of fluorescence emission	Eq. (S7d)
$\Phi_{F_{\max}}$	The maximum fluorescence quantum yield of PSII obtained with fully dark-adapted leaves.	Eq. (21c)
$\text{ChlF}_{\text{PSII}_{\max}}$	Broadband chlorophyll fluorescence emission from PSII presented Corresponding to the maximum fluorescence yield obtained with fully dark-adapted leaves.	Observed
NPQ	Nonphotochemical quenching, equating to $K_N/(K_F + K_D)$	Eq. (20)
J	Linear electron transport	Eq. (7)
Γ^*	Chloroplastic compensation point of CO_2	Eq. (22)
C_c	Chloroplastic CO_2 partial pressure	Eqs. (24)–(28)
T_{air}	Air temperature	Observed
SWC	Soil volumetric water content	Observed
PAR	Incoming photosynthetically active radiation	Observed

Appendix B. Supplementary data

Supplementary data to this article can be found online at <https://doi.org/10.1016/j.rse.2022.112893>.

References

- Atherton, J., Nichol, C.J., Porcar-Castell, A., 2016. Using spectral chlorophyll fluorescence and the photochemical reflectance index to predict physiological dynamics. *Remote Sens. Environ.* 176, 17–30.
- Bacour, C., Maignan, F., MacBean, N., Porcar-Castell, A., Flexas, J., Frankenberg, C., Peylin, P., Chevallier, F., Vuichard, N., Bastrikov, V., 2019. Improving estimates of gross primary productivity by assimilating solar-induced fluorescence satellite retrievals in a terrestrial biosphere model using a process-based SIF model. *J. Geophys. Res. Biogeosci.* 124, 3281–3306.
- Badgley, G., Field, C.B., Berry, J.A., 2017. Canopy near-infrared reflectance and terrestrial photosynthesis. *Sci. Adv.* 3, e1602244.
- Bilger, W., Björkman, O., 1990. Role of the xanthophyll cycle in photoprotection elucidated by measurements of light-induced absorbance changes, fluorescence and photosynthesis in leaves of *Hedera canariensis*. *Photosynth. Res.* 25, 173–185.
- Bonan, G.B., 1995. Land-atmosphere CO₂ exchange simulated by a land surface process model coupled to an atmospheric general circulation model. *J. Geophys. Res.* 100, 2817.
- Chang, C.Y., Guanter, L., Frankenberg, C., Köhler, P., Gu, L., Magney, T.S., Grossmann, K., Sun, Y., 2020. Systematic assessment of retrieval methods for canopy far-red solar-induced chlorophyll fluorescence using high-frequency automated field spectroscopy. *J. Geophys. Res. Biogeosci.* 125, e2019JG005533–e002019JG005533.
- Chen, J.M., Liu, J., Cihlar, J., Goulden, M.L., 1999. Daily canopy photosynthesis model through temporal and spatial scaling for remote sensing applications. *Ecol. Model.* 124, 99–119.
- Collatz, G.J., Ball, J.T., Grivet, C., Berry, J.A., 1991. Physiological and environmental regulation of stomatal conductance, photosynthesis and transpiration: a model that includes a laminar boundary layer. *Agric. For. Meteorol.* 54, 107–136.
- Desai, A.R., Noormets, A., Bolstad, P.V., Chen, J., Cook, B.D., Davis, K.J., Euskirchen, E. S., Gough, C., Martin, J.G., Ricciuto, D.M., Schmid, H.P., Tang, J., Wang, W., 2008. Influence of vegetation and seasonal forcing on carbon dioxide fluxes across the upper Midwest, USA: implications for regional scaling. *Agric. For. Meteorol.* 148, 288–308.
- Du, S.S., Liu, L.Y., Liu, X.J., Hu, J.C., 2017. Response of canopy solar-induced chlorophyll fluorescence to the absorbed photosynthetically active radiation absorbed by chlorophyll. *Remote Sens.* 9, 911.
- Du, S., Liu, L., Liu, X., Zhang, X., Gao, X., Wang, W., 2020. The solar-induced chlorophyll fluorescence imaging spectrometer (SIFIS) onboard the first terrestrial ecosystem carbon inventory satellite (TECIS-1): specifications and prospects. *Sensors* 20, 815.
- Falge, E., Baldocchi, D., Olson, R., Anthoni, P., Aubinet, M., Bernhofer, C., Burba, G., Ceulemans, R., Clement, R., Dolman, H., Granier, A., Gross, P., Grünwald, T., Hollinger, D., Jensen, N.-O., Katul, G., Keronen, P., Kowalski, A., Lai, C.T., Law, B.E., Meyers, T., Moncrieff, J., Moors, E., Munger, J.W., Pilegaard, K., Rannik, Ü., Rebmann, C., Suyker, A., Tenhunen, J., Tu, K., Verma, S., Vesala, T., Wilson, K., Wofsy, S., 2001. Gap filling strategies for defensible annual sums of net ecosystem exchange. *Agric. For. Meteorol.* 107, 43–69.
- Flexas, J., Escalona, J.M., Evain, S., Gulías, J., Moya, I., Osmond, C.B., Medrano, H., 2002. Steady-state chlorophyll fluorescence (Fs) measurements as a tool to follow variations of net CO₂ assimilation and stomatal conductance during water-stress in C₃ plants. *Physiol. Plant.* 114, 231–240.
- Franck, F., Juneau, P., Popovic, R., 2002. Resolution of the photosystem I and photosystem II contributions to chlorophyll fluorescence of intact leaves at room temperature. *Biochim. Biophys. Acta (BBA) - Bioenergetics* 1556, 239–246.
- Frankenberg, C., O'Dell, C., Berry, J., Guanter, L., Joiner, J., Koehler, P., Pollock, R., Taylor, T.E., 2014. Prospects for chlorophyll fluorescence remote sensing from the orbiting carbon observatory-2. *Remote Sens. Environ.* 147, 1–12.
- Galmés, J., Medrano, H., Flexas, J., 2007. Photosynthetic limitations in response to water stress and recovery in Mediterranean plants with different growth forms. *New Phytol.* 175, 81–93.
- Genty, B., Briantais, J.M., Baker, N.R., 1989. The relationship between the quantum yield of photosynthetic electron transport and quenching of chlorophyll fluorescence. *Biochim. Biophys. Acta Gen. Subj.* 990, 87–92.
- Gitelson, A.A., 2004. Wide dynamic range vegetation index for remote quantification of biophysical characteristics of vegetation. *J. Plant Physiol.* 161, 165–173.
- Gitelson, A.A., Buschmann, C., Lichtenthaler, H.K., 1998. Leaf chlorophyll fluorescence corrected for re-absorption by means of absorption and reflectance measurements. *J. Plant Physiol.* 152, 283–296.
- Gu, L., Sun, Y., 2014. Artefactual responses of mesophyll conductance to CO₂ and irradiance estimated with the variable J and online isotope discrimination methods. *Plant Cell Environ.* 37, 1231–1249.
- Gu, L., Han, J., Wood, J.D., Chang, C.Y.Y., Sun, Y., 2019a. Sun-induced Chl fluorescence and its importance for biophysical modeling of photosynthesis based on light reactions. *New Phytol.* 223, 1179–1191.
- Gu, L., Wood, J.D., Chang, C.Y.Y., Sun, Y., Riggs, J.S., 2019b. Advancing terrestrial ecosystem science with a novel automated measurement system for sun-induced chlorophyll fluorescence for integration with Eddy covariance flux networks. *J. Geophys. Res. Biogeosci.* 124, 127–146.
- Guanter, L., Frankenberg, C., Dudhia, A., Lewis, P.E., Gomez-Dans, J., Kuze, A., Suto, H., Grainger, R.G., 2012. Retrieval and global assessment of terrestrial chlorophyll fluorescence from GOSAT space measurements. *Remote Sens. Environ.* 121, 236–251.
- Guanter, L., Rossini, M., Colombo, R., Meroni, M., Frankenberg, C., Lee, J.-E., Joiner, J., 2013. Using field spectroscopy to assess the potential of statistical approaches for the retrieval of sun-induced chlorophyll fluorescence from ground and space. *Remote Sens. Environ.* 133, 52–61.
- He, L., Magney, T., Dutta, D., Yin, Y., Köhler, P., Grossmann, K., Stutz, J., Dold, C., Hatfield, J., Guan, K., Peng, B., Frankenberg, C., 2020. From the ground to space: using solar-induced chlorophyll fluorescence to estimate crop productivity. *Geophys. Res. Lett.* 47, e2020GL087474–e082020GL087474.
- Hendrickson, L., Furbank, R.T., Chow, W.S., 2004. A simple alternative approach to assessing the fate of absorbed light energy using chlorophyll fluorescence. *Photosynth. Res.* 82, 73.
- Ju, W., Chen, J.M., Black, T.A., Barr, A.G., Liu, J., Chen, B., 2006. Modelling multi-year coupled carbon and water fluxes in a boreal aspen forest. *Agric. For. Meteorol.* 140, 136–151.
- June, T., Evans, J.R., Farquhar, G.D., 2004. A simple new equation for the reversible temperature dependence of photosynthetic electron transport: a study on soybean leaf. *Funct. Plant Biol.* 31, 275.
- Kattge, J., Knorr, W., 2007. Temperature acclimation in a biochemical model of photosynthesis: a reanalysis of data from 36 species. *Plant Cell Environ.* 30, 1176–1190.
- Katul, G., Manzoni, S., Palmroth, S., Oren, R., 2010. A stomatal optimization theory to describe the effects of atmospheric CO₂ on leaf photosynthesis and transpiration. *Ann. Bot.* 105, 431–442.
- Kimball, J.S., Thornton, P.E., White, M.A., Running, S.W., 1997. Simulating forest productivity and surface-atmosphere carbon exchange in the BOREAS study region. *Tree Physiol.* 17, 589–599.
- Kimm, H., Guan, K., Burroughs, C.H., Peng, B., Ainsworth, E.A., Bernacchi, C.J., Moore, C.E., Kumagai, E., Yang, X., Berry, J.A., Wu, G., 2021. Quantifying high-temperature stress on soybean canopy photosynthesis: the unique role of sun-induced chlorophyll fluorescence. *Glob. Chang. Biol.* 27, 2403–2415.
- Koffi, E.N., Rayner, P.J., Norton, A.J., Frankenberg, C., Scholze, M., 2015. Investigating the usefulness of satellite-derived fluorescence data in inferring gross primary productivity within the carbon cycle data assimilation system. *Biogeosciences* 12, 4067–4084.
- Kramer, D.M., Johnson, G., Kiirats, O., Edwards, G.E., 2004. New fluorescence parameters for the determination of QA redox state and excitation energy fluxes. *Photosynth. Res.* 79, 209.
- Lasslop, G., Reichstein, M., Papale, D., Richardson, A.D., Arneeth, A., Barr, A., Stoy, P., Wohlfahrt, G., 2010. Separation of net ecosystem exchange into assimilation and respiration using a light response curve approach: critical issues and global evaluation. *Glob. Chang. Biol.* 16, 187–208.
- Lazár, D., 2015. Parameters of photosynthetic energy partitioning. *J. Plant Physiol.* 175, 131–147.
- Lee, J.-E., Berry, J.A., van der Tol, C., Yang, X., Guanter, L., Damm, A., Baker, I., Frankenberg, C., 2015. Simulations of chlorophyll fluorescence incorporated into the community land model version 4. *Glob. Chang. Biol.* 21, 3469–3477.
- Liu, Y., Parolari, A.J., Kumar, M., Huang, C.-W., Katul, G.G., Porporato, A., 2017. Increasing atmospheric humidity and CO₂ concentration alleviate forest mortality risk. *Proc. Natl. Acad. Sci.* 114, 9918–9923.
- Liu, X., Guanter, L., Liu, L., Damm, A., Malenovsky, Z., Rascher, U., Peng, D., Du, S., Gastellu-Etchegorry, J.-P., 2019. Downscaling of solar-induced chlorophyll fluorescence from canopy level to photosystem level using a random forest model. *Remote Sens. Environ.* 231, 110772.
- Liu, X., Liu, L., Hu, J., Guo, J., Du, S., 2020. Improving the potential of red SIF for estimating GPP by downscaling from the canopy level to the photosystem level. *Agric. For. Meteorol.* 281, 107846.
- Liu, X., Liu, Z., Liu, L., Lu, X., Chen, J., Du, S., Zou, C., 2021. Modelling the influence of incident radiation on the SIF-based GPP estimation for maize. *Agric. For. Meteorol.* 307, 108522.
- Lloyd, J., Taylor, J.A., 1994. On the temperature dependence of soil respiration. *Funct. Ecol.* 8, 315.
- Long, S.P., Bernacchi, C.J., 2003. Gas exchange measurements, what can they tell us about the underlying limitations to photosynthesis? Procedures and sources of error. *J. Exp. Bot.* 54, 2393–2401.
- Lu, X., Liu, Z., Zhao, F., Tang, J., 2020. Comparison of total emitted solar-induced chlorophyll fluorescence (SIF) and top-of-canopy (TOC) SIF in estimating photosynthesis. *Remote Sens. Environ.* 251, 112083.
- Magney, T.S., Frankenberg, C., Fisher, J.B., Sun, Y., North, G.B., Davis, T.S., Kornfeld, A., Siebke, K., 2017. Connecting active to passive fluorescence with photosynthesis: a method for evaluating remote sensing measurements of Chl fluorescence. *New Phytol.* 215, 1594–1608.
- Magney, T.S., Bowling, D.R., Logan, B.A., Grossmann, K., Stutz, J., Blanken, P.D., Burns, S.P., Cheng, R., Garcia, M.A., Köhler, P., Lopez, S., Parazoo, N.C., Racza, B., Schimel, D., Frankenberg, C., 2019a. Mechanistic evidence for tracking the seasonality of photosynthesis with solar-induced fluorescence. *Proc. Natl. Acad. Sci.* 201900278.

- Magney, T.S., Frankenberg, C., Köhler, P., North, G., Davis, T.S., Dold, C., Dutta, D., Fisher, J.B., Grossmann, K., Harrington, A., Hatfield, J., Stutz, J., Sun, Y., Porcar-Castell, A., 2019b. Disentangling changes in the spectral shape of chlorophyll fluorescence: implications for remote sensing of photosynthesis. *J. Geophys. Res. Biogeosci.* 124, 1491–1507.
- Maxwell, K., Johnson, G.N., 2000. Chlorophyll fluorescence—a practical guide. *J. Exp. Bot.* 51, 659–668.
- Meeker, E.W., Magney, T.S., Bambach, N., Momayyezi, M., McElrone, A.J., 2021. Modification of a gas exchange system to measure active and passive chlorophyll fluorescence simultaneously under field conditions. *AoB PLANTS* 13.
- Meroni, M., Picchi, V., Rossini, M., Cogliati, S., Panigada, C., Nali, C., Lorenzini, G., Colombo, R., 2008. Leaf level early assessment of ozone injuries by passive fluorescence and photochemical reflectance index. *Int. J. Remote Sens.* 29, 5409–5422.
- Meroni, M., Rossini, M., Guanter, L., Alonso, L., Rascher, U., Colombo, R., Moreno, J., 2019. Remote sensing of solar-induced chlorophyll fluorescence: review of methods and applications. *Remote Sens. Environ.* 113, 2037–2051.
- Mohammed, G.H., Colombo, R., Middleton, E.M., Rascher, U., van der Tol, C., Nedbal, L., Goulas, Y., Pérez-Priego, O., Damm, A., Meroni, M., Joiner, J., Cogliati, S., Verhoef, W., Malenovsky, Z., Gastellu-Etcheberry, J.-P., Miller, J.R., Guanter, L., Moreno, J., Moya, I., Berry, J.A., Frankenberg, C., Zarco-Tejada, P.J., 2019. Remote sensing of solar-induced chlorophyll fluorescence (SIF) in vegetation: 50 years of progress. *Remote Sens. Environ.* 231, 111177.
- Palombi, L., Cecchi, G., Lognoli, D., Raimondi, V., Toci, G., Agati, G., 2011. A retrieval algorithm to evaluate the photosystem I and photosystem II spectral contributions to leaf chlorophyll fluorescence at physiological temperatures. *Photosynth. Res.* 108, 225–239.
- Pedrés, R., Moya, I., Goulas, Y., Jacquemoud, S., 2008. Chlorophyll fluorescence emission spectrum inside a leaf. *Photochem. Photobiol. Sci.* 7, 498–502.
- Pedrés, R., Goulas, Y., Jacquemoud, S., Louis, J., Moya, I., 2010. FluorMODleaf: a new leaf fluorescence emission model based on the PROSPECT model. *Remote Sens. Environ.* 114, 155–167.
- Pfündel, E.E., 2021. Simultaneously measuring pulse-amplitude-modulated (PAM) chlorophyll fluorescence of leaves at wavelengths shorter and longer than 700 nm. *Photosynth. Res.* 147, 345–358.
- Pfündel, E.E., Klughammer, C., Meister, A., Cerovic, Z.G., 2013. Deriving fluorometer-specific values of relative PSI fluorescence intensity from quenching of F0 fluorescence in leaves of *Arabidopsis thaliana* and *Zea mays*. *Photosynth. Res.* 114, 189–206.
- Porcar-Castell, A., 2011. A high-resolution portrait of the annual dynamics of photochemical and non-photochemical quenching in needles of *Pinus sylvestris*. *Physiol. Plant.* 143, 139–153.
- Porcar-Castell, A., Bäck, J., Juurola, E., Hari, P., 2006. Dynamics of the energy flow through photosystem II under changing light conditions: a model approach. *Funct. Plant Biol.* 33, 229.
- Porcar-Castell, A., Tyystjärvi, E., Atherton, J., van der Tol, C., Flexas, J., Pfündel, E.E., Moreno, J., Frankenberg, C., Berry, J.A., 2014. Linking chlorophyll a fluorescence to photosynthesis for remote sensing applications: mechanisms and challenges. *J. Exp. Bot.* 65, 4065–4095.
- Porcar-Castell, A., Malenovsky, Z., Magney, T., Van Wittenberghe, S., Fernández-Marín, B., Maignan, F., Zhang, Y., Maseyk, K., Atherton, J., Albert, L.P., Robson, T. M., Zhao, F., Garcia-Plazaola, J.-I., Ensminger, I., Rajewicz, P.A., Grebe, S., Tikkanen, M., Kellner, J.R., Ihalainen, J.A., Rascher, U., Logan, B., 2021. Chlorophyll a fluorescence illuminates a path connecting plant molecular biology to earth-system science. *Nat. Plants* 7, 998–1009.
- Qiu, B., Li, W., Wang, X., Shang, L., Song, C., Guo, W., Zhang, Y., 2019. Satellite-observed solar-induced chlorophyll fluorescence reveals higher sensitivity of alpine ecosystems to snow cover on the Tibetan Plateau. *Agric. For. Meteorol.* 271, 126–134.
- Reichstein, M., Falge, E., Baldocchi, D., Papale, D., Aubinet, M., Berbigier, P., Bernhofer, C., Buchmann, N., Gilmanov, T., Granier, A., Grunwald, T., Havrankova, K., Ilvesniemi, H., Janous, D., Knohl, A., Laurila, T., Lohila, A., Loustau, D., Matteucci, G., Meyers, T., Miglietta, F., Ourcival, J.M., Pumpanen, J., Rambal, S., Rotenberg, E., Sanz, M., Tenhunen, J., Seufert, G., Vaccari, F., Vesala, T., Yakir, D., Valentini, R., 2005. On the separation of net ecosystem exchange into assimilation and ecosystem respiration: review and improved algorithm. *Glob. Chang. Biol.* 11, 1424–1439.
- Rosema, A., Snel, J.F.H., Zahn, H., Buurmeijer, W.F., Van Hove, L.W.A., 1998. The relation between laser-induced chlorophyll fluorescence and photosynthesis. *Remote Sens. Environ.* 65, 143–154.
- Siegmann, B., Cendrero-Mateo, M.P., Cogliati, S., Damm, A., Gamon, J., Herrera, D., Jedmowski, C., Junker-Frohn, L.V., Kraska, T., Müller, O., Rademske, P., van der Tol, C., Quiros-Vargas, J., Yang, P., Rascher, U., 2021. Downscaling of far-red solar-induced chlorophyll fluorescence of different crops from canopy to leaf level using a diurnal data set acquired by the airborne imaging spectrometer HyPlant. *Remote Sens. Environ.* 264, 112609.
- van der Tol, C., Verhoef, W., Rosema, A., 2009. A model for chlorophyll fluorescence and photosynthesis at leaf scale. *Agric. For. Meteorol.* 149, 96–105.
- van der Tol, C., Berry, J.A., Campbell, P.K.E., Rascher, U., 2014. Models of fluorescence and photosynthesis for interpreting measurements of solar-induced chlorophyll fluorescence. *J. Geophys. Res. Biogeosci.* 119, 2312–2327.
- von Caemmerer, S., 2000. *Biochemical Models of Leaf Photosynthesis*. CSIRO Publishing.
- Wagle, P., Kakani, V.G., 2014. Seasonal variability in net ecosystem carbon dioxide exchange over a young Switchgrass stand. *GCB Bioenergy* 6, 339–350.
- Wagle, P., Gowda, P.H., Manjunatha, P., Northup, B.K., Rocateli, A.C., Taghvaeian, S., 2019. Carbon and water dynamics in co-located winter wheat and canola fields in the U.S. southern Great Plains. *Agric. For. Meteorol.* 279, 107714.
- Wang, Y.P., Leuning, R., 1998. A two-leaf model for canopy conductance, photosynthesis and partitioning of available energy I. *Agric. For. Meteorol.* 91, 89–111.
- Wang, Y., Cai, H., Yu, L., Peng, X., Xu, J., Wang, X., 2020. Evapotranspiration partitioning and crop coefficient of maize in dry semi-humid climate regime. *Agric. Water Manag.* 236, 106164.
- Wu, A., Hammer, G.L., Doherty, A., von Caemmerer, S., Farquhar, G.D., 2019. Quantifying impacts of enhancing photosynthesis on crop yield. *Nat. Plants* 5, 380–388.
- Wutzler, T., Lucas-Moffat, A., Migliavacca, M., Knauer, J., Sickel, K., Šigut, L., Menzer, O., Reichstein, M., 2018. Basic and extensible post-processing of eddy covariance flux data with REddyProc. *Biogeosciences* 15, 5015–5030.
- Xiao, J., Davis, K.J., Urban, N.M., Keller, K., Saliendra, N.Z., 2011. Upscaling carbon fluxes from towers to the regional scale: influence of parameter variability and land cover representation on regional flux estimates. *J. Geophys. Res.* 116, G03027.
- Yang, X., Tang, J., Mustard, J.F., Lee, J.-E., Rossini, M., Joiner, J., Munger, J.W., Kornfeld, A., Richardson, A.D., 2015. Solar-induced chlorophyll fluorescence that correlates with canopy photosynthesis on diurnal and seasonal scales in a temperate deciduous forest. *Geophys. Res. Lett.* 42, 2977–2987.
- Yang, P., van der Tol, C., Campbell, P.K.E., Middleton, E.M., 2020. Fluorescence correction vegetation index (FCVI): a physically based reflectance index to separate physiological and non-physiological information in far-red sun-induced chlorophyll fluorescence. *Remote Sens. Environ.* 240, 111676.
- Yin, X., Striik, P.C., 2009. C 3 and C 4 photosynthesis models: an overview from the perspective of crop modelling. *NJAS: Wageningen J. Life Sci.* 57, 27–38.
- Yu, L., Zeng, Y., Su, Z., Cai, H., Zheng, Z., 2016. The effect of different evapotranspiration methods on portraying soil water dynamics and ET partitioning in a semi-arid environment in Northwest China. *Hydrol. Earth Syst. Sci.* 20, 975–990.
- Zaks, J., Amarnath, K., Kramer, D.M., Niyogi, K.K., Fleming, G.R., 2012. A kinetic model of rapidly reversible nonphotochemical quenching. *Proc. Natl. Acad. Sci. U. S. A.* 109, 15757–15762.
- Zeng, Y., Badgley, G., Dechant, B., Ryu, Y., Chen, M., Berry, J.A., 2019. A practical approach for estimating the escape ratio of near-infrared solar-induced chlorophyll fluorescence. *Remote Sens. Environ.* 232, 111209.
- Zhang, C., Atherton, J., Peñuelas, J., Filella, I., Kolari, P., Aalto, J., Ruhanen, H., Bäck, J., Porcar-Castell, A., 2019. Do all chlorophyll fluorescence emission wavelengths capture the spring recovery of photosynthesis in boreal evergreen foliage? *Plant Cell Environ.* 42, 3264–3279.
- Zhao, F., Guo, Y., Verhoef, W., Gu, X., Liu, L., Yang, G., 2014. A method to reconstruct the solar-induced canopy fluorescence Spectrum from Hyperspectral measurements. *Remote Sens.* 6, 10171–10192.